



Publication Year	2016
Acceptance in OA @INAF	2021-04-23T13:38:11Z
Title	Electromagnetic Emission from Long-lived Binary Neutron Star Merger Remnants. I. Formulation of the Problem
Authors	Siegel, Daniel M.; CIOLFI, RICCARDO
DOI	10.3847/0004-637X/819/1/14
Handle	http://hdl.handle.net/20.500.12386/30883
Journal	THE ASTROPHYSICAL JOURNAL
Number	819



ELECTROMAGNETIC EMISSION FROM LONG-LIVED BINARY NEUTRON STAR MERGER REMNANTS. I. FORMULATION OF THE PROBLEM

DANIEL M. SIEGEL¹ AND RICCARDO CIOLFI^{2,3}

¹ Max Planck Institute for Gravitational Physics (Albert Einstein Institute), Am Mühlenberg 1, D-14476 Potsdam-Golm, Germany;
daniel.siegel@aei.mpg.de

² Physics Department, University of Trento, Via Sommarive 14, I-38123 Trento, Italy; riccardo.ciolfi@unitn.it

³ INFN-TIFPA, Trento Institute for Fundamental Physics and Applications, Via Sommarive 14, I-38123 Trento, Italy
Received 2015 September 3; accepted 2015 December 16; published 2016 February 24

ABSTRACT

Binary neutron star (BNS) mergers are the leading model to explain the phenomenology of short gamma-ray bursts (SGRBs). Recent observations of long-lasting X-ray afterglows of SGRBs challenge standard paradigms and indicate that in a large fraction of events a long-lived neutron star (NS) may be formed rather than a black hole. Understanding the mechanisms underlying these afterglows is necessary in order to address the open questions concerning the nature of SGRB central engines. However, recent theoretical progress has been hampered by the fact that the timescales of interest for the afterglow emission are inaccessible to numerical relativity simulations. Here we present a detailed model to bridge the gap between numerical simulations of the merger process and the relevant timescales for the afterglows, assuming that the merger results in a long-lived NS. This model is formulated in terms of a set of coupled differential equations that follow the evolution of the post-merger system and predict its electromagnetic (EM) emission in a self-consistent way, starting from initial data that can be extracted from BNS merger simulations. The model presented here also allows us to search for suitable EM counterparts for multimessenger astronomy, which is expected to become reality within the next few years thanks to ground-based GW detectors such as advanced LIGO and Virgo. This paper discusses the formulation and implementation of the model. In a companion paper, we employ this model to predict the EM emission from $\sim 10^{-2}$ to $\sim 10^7$ s after a BNS merger and discuss the implications in the context of SGRBs and multimessenger astronomy.

Key words: gamma-ray burst: general – gravitational waves – pulsars: general – radiation mechanisms: general – stars: magnetars – stars: neutron

1. INTRODUCTION

The coalescence of binary neutron stars (BNS) represents the most promising source of gravitational waves (GWs) for the detection with ground-based interferometric detectors such as advanced LIGO and Virgo (Harry et al. 2010; Accadia et al. 2011). At the same time, BNS mergers are responsible for observable electromagnetic (EM) emission that carries complementary information on the source and that can be combined with the GW detection to significantly enlarge the scientific output. As an independent observational channel, EM signals provide positional and temporal information that can enhance the search sensitivity of the GW detectors and lead to GW detections (e.g., Abadie et al. 2012b; Aasi et al. 2014; Clark et al. 2015; Williamson et al. 2014). Inversely, EM follow-up observations triggered by a GW detection can confirm the astrophysical origin of the event (e.g., Abadie et al. 2012a; Evans et al. 2012; Singer et al. 2014), provided a suitable, characteristic EM counterpart signal can be identified with the merger and/or post-merger phase of the evolution of the BNS system. In addition, EM counterparts can constrain physical properties of the BNS merger remnant and its dynamics that cannot be probed by GW observations (e.g., magnetic fields, mass ejection). In the case of a confident GW detection, important constraints on the source properties, the EM emission mechanisms, and the energetics involved can be obtained even from a non-detection of an EM counterpart. Moreover, detecting such EM signals could significantly improve the sky localization of the source and thus the identification of the host galaxy, allowing for two independent measurements of the redshift and the Hubble constant (e.g.,

Schutz 1986; Metzger & Berger 2012; Berger 2014). Furthermore, joint EM and GW observations can reveal important information on when and how short gamma-ray bursts (SGRBs) can be produced in BNS mergers. In particular, they can verify or falsify the recently proposed “time-reversal” scenario for SGRBs and possibly provide a very accurate method to determine the lifetime of a remnant NS and to place strong constraints on the unknown equation of state of nuclear matter at high densities (Ciolfi & Siegel 2015a, 2015b). With the advanced LIGO/Virgo detector network starting their first science runs later this year, such multimessenger astronomy will become reality in the very near future. The actual benefit of joint GW and EM observations, however, depends on our knowledge of the expected EM signals associated with BNS mergers and the underlying physical mechanisms, which are still poorly understood. Therefore, a deeper understanding of these EM signals is urgently needed.

BNS mergers are commonly considered the leading scenario to explain the phenomenology of SGRBs (e.g., Paczynski 1986; Eichler et al. 1989; Narayan et al. 1992; Barthelmy et al. 2005; Fox et al. 2005; Gehrels 2005; Shibata et al. 2006; Rezzolla et al. 2011; Paschalidis et al. 2015). Currently, very strong evidence for the association of SGRBs with BNS or neutron star–black hole (NS–BH) mergers comes from the recent detection of possible radioactively powered kilonova events (e.g., Li & Paczyński 1998; Kulkarni 2005; Rosswog 2005; Metzger et al. 2010; Berger et al. 2013; Tanvir et al. 2013; Yang et al. 2015). While this is still a matter of debate, joint EM and GW observations will provide a powerful tool to unambiguously confirm the association of SGRBs with

compact object coalescence. For this reason, the prompt γ -ray emission of SGRBs lasting less than ≈ 2 s has so far been the prime target of studies on joint EM and GW observations (e.g., Abadie et al. 2012a, 2012b; Evans et al. 2012; Aasi et al. 2014; Clark et al. 2015; Singer et al. 2014; Williamson et al. 2014).

Nevertheless, the SGRB prompt emission is thought to be collimated and will thus be beamed away from the observer in most cases (see Berger 2014 for an overview of observations to date; see also Section 7 of Siegel & Ciolfi 2016). During many years of observations, including the 10 years of operation of the *Swift* satellite (Gehrels et al. 2004), no SGRB with known redshift has been detected within the sensitivity volume of advanced LIGO/Virgo. Furthermore, joint EM and GW observations are so far based on the assumption that the EM and the GW signals are characterized by a relative time lag of at most a few seconds. However, the details of how the prompt emission in SGRBs is generated still remain unclear, and the burst could, e.g., be generated a long time ($\sim 10^2$ – 10^4 s) after the merger (Ciolfi & Siegel 2015a, 2015b). In the latter case, joint observations focusing on a time window of a few seconds around the time of merger would miss the SGRB. Likewise, focusing on a time lag of a few seconds around a detected SGRB could lead to a non-detection of GW emission. Hence, when assuming coincidence within a short time window around the time of merger, one has to be cautious when drawing astrophysical conclusions in either case. Finally, even if a SGRB is observed in coincidence with a GW signal, such an observation alone will unlikely be able to distinguish between a BNS and a NS–BH merger, as the SGRB emission is expected to be very similar for both progenitor models (see below). It is therefore important to identify bright, long-lasting and highly isotropic EM counterparts that are produced in a high fraction of events and that can distinguish between a BNS and a NS–BH progenitor system.

A standard model to explain the generation of the SGRB prompt emission in BNS and NS–BH mergers is an accretion powered relativistic jet from a BH–torus system that is formed soon ($\lesssim 10$ – 100 ms) after merger (e.g., Narayan et al. 1992; Shibata et al. 2006; Rezzolla et al. 2011; Paschalidis et al. 2015). This accretion process and the resulting energy release cease once the torus has been accreted on a timescale of at most one second, which is consistent with the typical timescale of the prompt SGRB emission ($\lesssim 2$ s). However, recent observations by the *Swift* satellite have revealed long-lasting X-ray afterglows in a large fraction of SGRB events that are indicative of ongoing energy ejection on much longer timescales up to $\sim 10^4$ s (Gompertz et al. 2013, 2014; Rowlinson et al. 2013; Lü et al. 2015). Even considering that the interaction of the jet with the interstellar medium might produce an afterglow signal lasting longer than the accretion timescale, persistent emission with a duration of $\sim 10^4$ s remains difficult to explain within this BH–torus scenario (Kumar & Zhang 2015 and references therein). A possible alternative is that a large fraction of BNS mergers lead to the formation of a stable or at least sufficiently long-lived NS rather than a BH–torus system (e.g., Zhang & Mészáros 2001; Metzger et al. 2008; Rowlinson et al. 2010; Bucciantini et al. 2012; Gompertz et al. 2013; Rowlinson et al. 2013; Zhang 2013; Lü et al. 2015). Such a long-lived NS can power ongoing energy ejection on the relevant timescales via loss of rotational energy. This is a clearly distinctive feature of BNS mergers as opposed to NS–BH mergers, which cannot produce a remnant

NS. NS–BH mergers are thus challenged as a progenitor model for at least a large class of SGRBs.

The formation of a long-lived NS is indeed a very likely outcome of a BNS merger. The merger product depends on the masses of the two progenitor NSs and the equation of state of nuclear matter at high densities, which is unknown. Recent observations of high-mass NSs (Demorest et al. 2010; Antoniadis et al. 2013) indicate a maximum gravitational mass for stable NSs of $M_{\text{TOV}} \gtrsim 2 M_{\odot}$. However, NSs with masses $M > M_{\text{TOV}}$ can be centrifugally supported against gravitational collapse by uniform rotation up to the mass-shedding limit, which is known as the supramassive regime. This results in a maximum mass for uniformly rotating configurations of $M_{\text{supra}} \approx 1.2 M_{\text{TOV}} \gtrsim 2.4 M_{\odot}$ (Lasota et al. 1996). Furthermore, the distribution of NSs in binary systems is sharply peaked around 1.3 – $1.4 M_{\odot}$, with the first born NS slightly more massive than the second one; this leads to a typical remnant NS mass of ≈ 2.3 – $2.4 M_{\odot}$ when accounting for neutrino losses and mass ejection (Belczynski et al. 2008). Progenitors of lighter NSs are much more abundant than progenitors for massive NSs, and population synthesis calculations show that 99% of all BNS mergers should lead to a remnant mass between ≈ 2.2 – $2.5 M_{\odot}$ (Belczynski et al. 2008). Hence, a supramassive NS should be a likely product of a BNS merger. Furthermore, some BNS mergers would lead to a slightly hypermassive NS (i.e., above the maximum mass supported by uniform rotation), which, however, could still migrate to a supramassive configuration through subsequent mass loss (cf. Section 4.1). Only a limited fraction of BNS mergers should promptly form a BH–torus system as assumed in the standard model.

EM emission from a long-lived remnant NS when applied to a large class of X-ray afterglows of SGRBs has so far been modeled in a simple way as dipole spin-down emission from a uniformly rotating magnetar (e.g., Gompertz et al. 2013; Rowlinson et al. 2013; Lü et al. 2015). This model assumes an instantaneous and direct conversion of spin-down luminosity L_{sd} into observed X-ray luminosity L_X by some unspecified process, $L_{\text{sd}} \propto L_X$, and consists of a simple analytically specified formula to fit the X-ray lightcurves. In particular, it does not take into account baryon pollution due to dynamical mass ejection and subsequent neutrino and magnetically driven winds (e.g., Oechslin et al. 2007; Dessart et al. 2009; Bauswein et al. 2013; Hotokezaka et al. 2013; Metzger & Fernández 2014; Siegel et al. 2014; Kastaun & Galeazzi 2015), which leads to a much more complex post-merger evolution (see, however, Metzger et al. 2008; Bucciantini et al. 2012). Based on a simple dynamical model, Yu et al. (2013) and Gao et al. (2015) have investigated EM emission from a long-lived millisecond magnetar surrounded by an envelope of previously ejected matter, finding a late-time brightening (termed “magnetar-driven macro-nova”) consistent with the optical and X-ray (re)brightening of GRB 080503. Based on a refined physical model, Metzger & Piro (2014) have investigated the evolution of a stable millisecond magnetar in a similar setup and reported late-time brightenings of the luminosity in the optical and X-ray band, compatible with features observed in GRB 080503 and GRB 130603B (see Section 6 for a comparison of these previous models to ours). Accurately modeling the EM emission from a long-lived remnant NS is challenging because of the complex physics involved (baryon pollution, thermal effects, neutrino emission, strong magnetic fields with complex structure, strong differential rotation) and

the wide range of timescales involved (from ms to days after the merger). While the early post-merger phase and thus the generation of the prompt SGRB emission can be probed by numerical relativity simulations, such typical timescales for EM afterglows are inaccessible to those simulations. On the other hand, semi-analytical modeling has so far concentrated on computing EM emission in the late-time regime ($\sim 10^3$ – 10^6 s after merger; Gao et al. 2013; Metzger & Piro 2014; Yu et al. 2013; Gao et al. 2015).

Here and in a companion Paper (Siegel & Ciolfi 2016, henceforth Paper II), we consider the likely case of a long-lived NS remnant and provide a dynamical model to self-consistently compute the EM emission of the post-merger system based on some initial data that can be extracted from a numerical relativity simulation tens of milliseconds after the merger. This model thus bridges the gap between the short timescales accessible to numerical relativity simulations and the timescales of interest for EM afterglow radiation as recorded by satellite missions like *Swift*. We note that our model does not include the EM emission associated with the formation of a relativistic jet, which can be added to the EM signal predicted here. The model is very general and should be applicable to any BNS merger that leads to the formation of a long-lived NS. As we have argued above, this should cover the vast majority of BNS merger events. Therefore, our model represents an important tool to study and identify promising EM counterparts of BNS mergers for coincident EM and GW observations as discussed above and to investigate the nature of long-lasting X-ray afterglows observed in a large fraction of SGRB events. The present paper is devoted to a detailed discussion of the physical model and its numerical implementation. In Paper II, we apply the model to a large number of possible long-lived BNS merger remnants, employing a wide range of physical input parameters. Our results and their astrophysical implications are discussed in Paper II.

This paper is organized as follows. Section 2 describes the phenomenology underlying our evolution model. In Section 3, we provide a brief summary of the model, which is formulated in terms of sets of highly coupled ordinary differential equations. The subsequent section describes the ingredients to these equations in detail. In Section 5, we discuss some numerical aspects for integrating the model equations and, in particular, present a scheme to reconstruct the observer lightcurves and spectra including relativistic beaming, the relativistic Doppler effect and the time-of-flight effect. Section 6 is devoted to discussion and conclusions. Several appendices are added to streamline the discussion in the main part of the paper.

2. PHENOMENOLOGY

This section is intended to provide a conceptual outline of the phenomenology our evolution model is built upon. We assume that a BNS merger leads to the formation of a long-lived NS and divide the post-merger evolution into three phases: an early baryonic-wind phase (Phase I; $t \lesssim 1$ – 10 s), a pulsar wind shock phase (Phase II; $t \sim 10$ s), and a pulsar wind nebula (PWN) phase (Phase III; ~ 10 s $\lesssim t \lesssim 10^7$ s). These evolution phases are depicted in Figure 1. Our model provides a self-consistent dynamical evolution once the physical properties of the system in the early post-merger phase are specified. These properties can be extracted or estimated from BNS merger simulations in general relativity. In particular, we

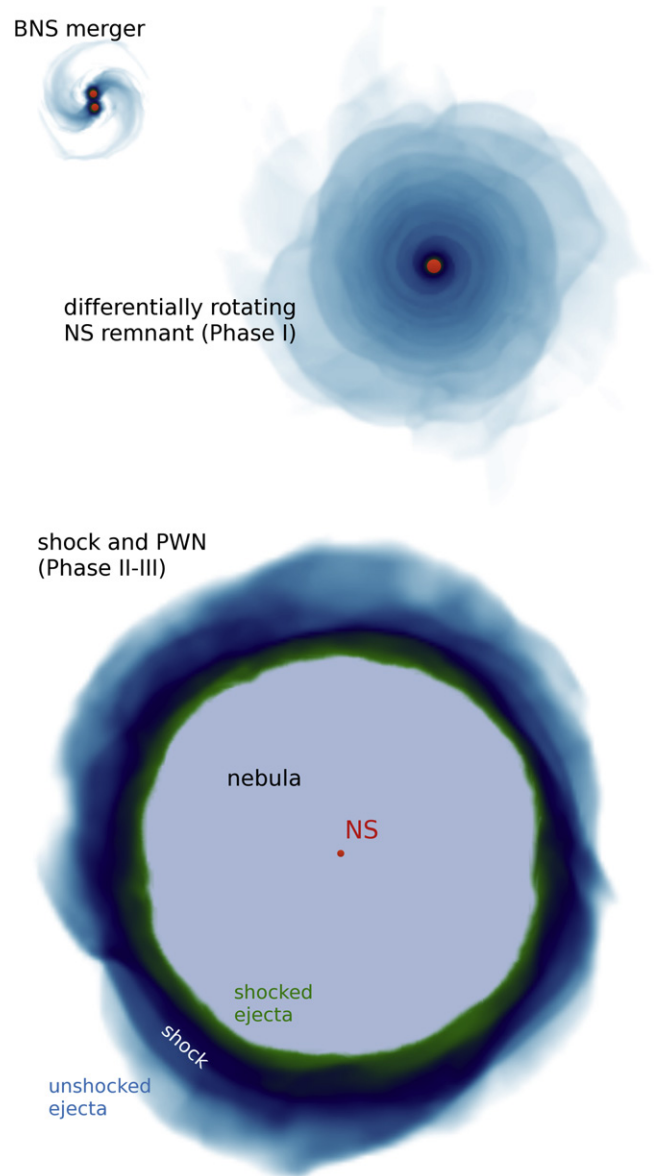


Figure 1. Evolution of the system according to the proposed scenario (with increasing spatial scale). A BNS merger (top left) forms a differentially rotating NS that emits a baryon-loaded wind (Phase I). The NS eventually settles down to uniform rotation and inflates a pulsar wind nebula (or simply “nebula”) that sweeps up all the ejecta material into a thin shell (Phase II). Spin-down emission from the NS continues while the nebula and the ejecta shell keep expanding (Phase III).

start the evolution at a few to tens of milliseconds after the BNS merger, once a roughly axisymmetric state of the remnant NS has been reached and the strong GW emission characterizing the merger phase has been severely damped.

In our reference scenario, Phase I starts with a supramassive NS, which is a very likely outcome of a BNS merger (see Section 1). Nevertheless, the phenomenology described here also applies if the NS is stable or if its mass is only slightly above the hypermassive limit, provided that in the latter case the star enters the supramassive regime through additional mass loss before collapsing to a black hole (see below).

The newly-born NS is differentially rotating and endowed with strong magnetic fields (up to magnetar field strengths) due to compression of the two progenitor stars and magnetic field

amplification mechanisms acting during the merger, such as the Kelvin-Helmholtz instability (e.g., Price & Rosswog 2006; Zrake & MacFadyen 2013; Giacomazzo et al. 2015). Moreover, further amplification occurs during Phase I, i.e., as long as differential rotation is active, via magnetic winding and possibly the magnetorotational instability (e.g., Duez et al. 2006; Siegel et al. 2013; Kiuchi et al. 2014). These latter mechanisms are likely to dominate the removal of differential rotation itself, which occurs on the timescale t_{dr} . In this case, t_{dr} is roughly given by the Alfvén timescale and can be as long as $t_{\text{dr}} \sim 1\text{--}10$ s for the objects considered here, depending on the initial magnetic field strength (Shapiro 2000).

At birth, the remnant star is already surrounded by material dynamically ejected during or shortly after the merger, with a total mass of up to $M_{\text{ej}} \lesssim 10^{-3} M_{\odot}$ (e.g., Bauswein et al. 2013; Hotokezaka et al. 2013; Kastaun & Galeazzi 2015; see the discussion in Section 4.1). However, additional mass ejection is expected to take place during Phase I, which can even dominate over this early dynamical outflow in terms of total ejected mass. One main mass ejection mechanism results from magnetic field amplification in the stellar interior, which causes a build-up of magnetic pressure in the outer layers of the star. This pressure rapidly overcomes the gravitational binding at the stellar surface, launching a strong baryon-loaded magnetized wind (Siegel et al. 2014; Siegel & Ciolfi 2015b). Furthermore, substantial mass loss can be caused by neutrino-induced winds over typical timescales for neutrino cooling of $t_{\nu} \lesssim 1$ s (Dessart et al. 2009). For both mechanisms, i.e., magnetically and neutrino-induced winds, we expect highly isotropic mass ejection. The material ejected from the NS surface is typically hot with temperatures of up to tens of MeV (Siegel et al. 2014; Kastaun & Galeazzi 2015), while further energy is carried by the wind in the form of a strong Poynting flux (Siegel et al. 2014). These winds transport material outward at speeds of at most $v_{\text{ej,in}} \lesssim 0.1c$, creating a hot and optically thick environment. EM emission from these radially expanding winds is expected to be predominantly thermal, due to the very high optical depths at these early times. However, because of the high optical depth, radiative energy loss is still rather inefficient.

As differential rotation is being removed on the timescale t_{dr} , the NS settles down to uniform rotation. Mass loss is suppressed and while the ejected matter keeps moving outward the density in the vicinity of the NS is expected to drop on roughly the same timescale. In the resulting essentially baryon-free environment the NS can set up a pulsar-like magnetosphere. Via dipole spin-down, the NS starts powering a highly relativistic, Poynting-flux dominated outflow of charged particles (mainly electrons and positrons; see Section 4.2.1) or “pulsar wind” at the expense of rotational energy. This occurs at a time $t = t_{\text{pul,in}}$ and marks the beginning of Phase II.

The pulsar wind inflates a PWN behind the less rapidly expanding ejecta, a plasma of electrons, positrons and photons (see Section 4.3.1 for a detailed discussion). As this PWN is highly overpressured with respect to the confining ejecta envelope, it drives a strong hydrodynamical shock into the fluid, which heats up the material upstream of the shock and moves radially outward at relativistic speeds, thereby sweeping up all the material behind the shock front into a thin shell. During this phase the system is composed of a NS (henceforth “pulsar” in Phase II and III) surrounded by an essentially

baryon-free PWN and a layer of confining ejecta material. The propagating shock front separates the ejecta material into an inner shocked part and an outer unshocked part (cf. Figures 1 and 2). While the shock front is moving outward across the ejecta, the unshocked matter layer still emits thermal radiation with increasing luminosity as the optical depth decreases. Initially, the expansion of the PWN nebula is highly relativistic and decelerates to non-relativistic speeds only when the shock front encounters high-density material in the outer ejecta layers. The total crossing time for the shock front is typically $\Delta t_{\text{shock}} = t_{\text{shock,out}} - t_{\text{pul,in}} \ll t_{\text{pul,in}}$, where $t_{\text{shock,out}}$ denotes the time when the shock reaches the outer surface. At this break-out time, a short burst-type non-thermal EM signal could be emitted that encodes the signature of particle acceleration at the shock front.

Phase III starts at $t = t_{\text{shock,out}}$. At this time, the entire ejecta material has been swept up into a thin shell of thickness Δ_{ej} (which we assume to be constant during the following evolution) that moves outward with speed v_{ej} (cf. Figure 2). In general, this speed is higher than the expansion speed of the baryon-loaded wind in Phase I ($v_{\text{ej,in}}$), as during shock propagation kinetic energy is deposited into the shocked ejecta. Rotational energy is extracted from the pulsar via dipole spin-down and it is reprocessed in the PWN via various radiative processes in analogy to pair plasmas in compact sources, such as active galactic nuclei (see Section 4.3.1 for a detailed discussion). Radiation escaping from the PWN ionizes the ejecta material, which thermalizes the radiation due to the optical depth still being very high. Only at much later times the ejecta layer eventually becomes transparent to radiation from the nebula, which gives rise to a transition from predominantly thermal to non-thermal emission spectra. We note that for reasons discussed in Section 5.6, the total luminosity of the system shows the characteristic $\propto t^{-2}$ behavior for dipole spin-down at late times $t \gg t_{\text{sd}}$, where t_{sd} is the spin-down timescale. However, when restricted to individual frequency bands, the late time behavior of the luminosity can significantly differ from a $\propto t^{-2}$ power law.

As the NS is most likely not indefinitely stable against gravitational collapse, it might collapse at any time during the evolution outlined above (see Section 4.4). If the NS is supramassive, the collapse is expected to occur within timescales of the order of $\sim t_{\text{sd}}$, for the spin-down timescale represents the time needed to remove a significant fraction of the rotational energy from the NS and thus of its rotational support against collapse. For typical parameters, the collapse occurs in Phase III. However, if the NS is hypermassive at birth and does not migrate to a supramassive configuration thereafter, it is expected to collapse already in Phase I (i.e., on the timescale for removal of differential rotation). Moreover, even a supramassive NS can collapse on timescales shorter than $\sim t_{\text{sd}}$, if the collapse is induced by a (magneto-)hydrodynamic instability.

Assuming that a SGRB and its afterglows are produced by a BNS system merging into a long-lived NS, the prompt burst can be associated either with the merger itself or with the delayed collapse of the remnant NS, as in the recently proposed “time-reversal” scenario (Ciolfi & Siegel 2015a, 2015b; see Rezzolla & Kumar 2015 for an alternative proposal). Both scenarios can be accommodated by the framework of our model. In the former case, the lightcurves and spectra we

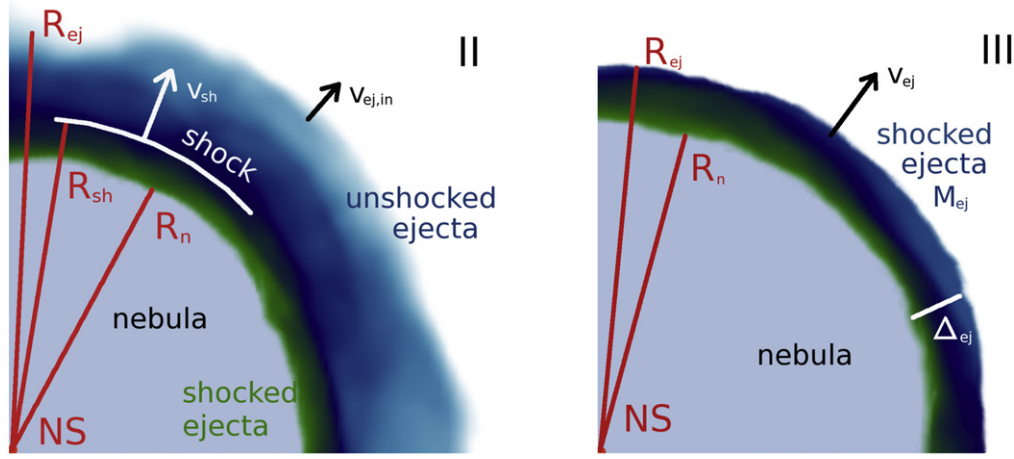


Figure 2. Left: phase II of the evolution. The high pressure of the pulsar wind nebula (“nebula”) powered by the spinning-down NS drives a strong shock through the ejecta with speed v_{sh} , thereby compressing, heating and accelerating the material. Right: phase III of the evolution. The ejecta material of mass M_{ej} has been entirely swept up by the shock into a thin layer of thickness Δ_{ej} moving outward at speed v_{ej} , while the spinning-down NS keeps injecting energy into the optically thick pulsar wind nebula.

predict after the time of merger represent a model for the observed afterglows. In the latter case, only the emission that follows the collapse should be directly compared with the observed afterglows. Predictions for both scenarios are discussed in detail in the companion paper (Paper II).

3. EVOLUTION EQUATIONS

According to the three main evolution phases discussed in Section 2, our model consists of three sets of coupled ordinary differential equations (ODEs), which we think capture the main physical ingredients to describe the dynamical evolution and EM emission of the post-merger system. These ODEs assume spherical symmetry and they are formulated in terms of main evolution quantities, such as the extent of certain dynamical structures (e.g., the baryon-loaded wind, the PWN and the ejecta shell) and their associated energy budgets. In summary, the evolution equations we consider are as follows (see Table 1 and Figure 2 for definitions of variables):

Phase I: baryon-loaded wind

$$\frac{dR_{ej}}{dt} = v_w(R_{ej}(t), t) \quad (1)$$

$$\frac{dE_{th}}{dt} = L_{EM}(t) + \frac{dE_{th,NS}}{dt} - L_{rad}(t) \quad (2)$$

Phase II: pulsar wind shock

$$\frac{dR_{ej}}{dt} = v_w(R_{ej}(t), t) \quad (3)$$

$$\frac{dR_{sh}}{dt} = v_{sh}(t) \quad (4)$$

$$\frac{dR_n}{dt} = \frac{dR_{sh}}{dt} - \frac{d\Delta_{sh}}{dt} \quad (5)$$

$$\frac{dE_{th,sh}}{dt} = \frac{dE_{sh}}{dt} + \frac{dE_{th,vol}}{dt} + \frac{dE_{PWN}}{dt} - L_{rad,in}(t) \quad (6)$$

$$\frac{dE_{th,ush}}{dt} = -\frac{dE_{th,vol}}{dt} - L_{rad}(t) \quad (7)$$

$$\frac{dE_{th}}{dt} = \frac{dE_{th,sh}}{dt} + \frac{dE_{th,ush}}{dt} \quad (8)$$

$$\frac{dE_{nth}}{dt} = -\frac{E_{nth}}{R_n} \frac{dR_n}{dt} - \frac{dE_{PWN}}{dt} + L_{rad,in}(t) + \eta_{TS}[L_{sd}(t) + L_{rad,pul}(t)] \quad (9)$$

$$\frac{dE_B}{dt} = \eta_{Bn}[L_{sd}(t) + L_{rad,pul}(t)] \quad (10)$$

Phase III: pulsar wind nebula

$$\frac{dv_{ej}}{dt} = a_{ej}(t) \quad (11)$$

$$\frac{dR_{ej}}{dt} = v_{ej}(t) + \frac{1}{2}a_{ej}(t)dt \quad (12)$$

$$\frac{dR_n}{dt} = \frac{dR_{ej}}{dt} \quad (13)$$

$$\frac{dE_{th}}{dt} = [1 - f_{ej}(t)] \frac{dE_{PWN}}{dt} - L_{rad}(t) - L_{rad,in}(t) \quad (14)$$

$$\frac{dE_B}{dt} = \eta_{Bn}[L_{sd}(t) + L_{rad,pul}(t)] \quad (15)$$

Equations (1) and (2) are supplemented with a model to describe the baryonic wind emitted from the NS during this phase (see Section 4.1.1). Furthermore, Equations (11)–(15) are supplemented with Equations (78) and (79), which model the radiative processes inside the PWN and which need to be solved at every time step of the evolution equations to determine the source term dE_{PWN}/dt and the emission spectrum of the nebula.

The above evolution equations are formulated in the rest frame of the merger remnant (henceforth the “lab frame”; see also Appendix A.2). The various terms appearing in Equations (1)–(15) are motivated and discussed in detail in Section 4.

4. INGREDIENTS.

4.1. Phase I: Baryon-loaded Wind

Phase I starts with a differentially rotating NS that generates a baryon-loaded wind, either due to a very strong magnetization of the stellar interior (Siegel et al. 2014) and/or as the result of neutrino emission from the stellar interior

Table 1
Definition of Lab-frame Quantities

Quantity	Description
t	time
R_{ej}	outer radius of the ejected matter
R_n	radius of the PWN (Phase II, III)
R_{sh}	radial location of the pulsar wind shock front (Phase II)
$v_w(r, t)$	velocity profile of the baryon-loaded wind (Phase I, II; cf. Section 4.1.1, Equation (30))
$v_{ej,in}$	initial expansion speed of the baryonic ejecta material (cf. Section 4.1.1, Equation (19))
v_{sh}	velocity of the pulsar wind shock front (Phase II; cf. Equation (58))
v_{ej}	velocity of the ejecta shell in Phase III (cf. Equation (95))
a_{ej}	acceleration of the ejecta shell in Phase III (cf. Equation (95))
Δ_{sh}	radial thickness of the shocked ejecta shell in Phase II (cf. Section 4.2.3)
Δ_{ej}	radial thickness of the ejecta shell in Phase III (cf. Section 4.3)
f_{ej}	function to smoothly ‘switch on/off’ terms as the ejecta material becomes optically thin (cf. Equation (102))
E_{th}	internal energy stored in the ejecta material, available to be emitted as thermal radiation
$E_{th,sh}$	internal energy stored in the shocked ejecta matter (Phase II)
$E_{th,ush}$	internal energy stored in the unshocked ejecta matter (Phase II)
E_{nth}	internal energy of the PWN
E_B	magnetic energy of the PWN
$dE_{th,NS}/dt$	internal energy injected from the NS into the baryon-loaded wind per unit time (Phase I; cf. Equation (33))
dE_{sh}/dt	energy deposited in the shocked ejecta material by shock heating per unit time (cf. Equation (63))
$dE_{th,vol}/dt$	total internal energy of unshocked ejecta in the volume swept up by the shock front per unit time (cf. Equation (62))
dE_{PWN}/dt	total energy emitted by the PWN per unit time (Phase II, III; cf. Equations (57) and (92))
L_{EM}	EM energy deposited in the baryon-loaded wind per unit time (Phase I; cf. Equation (32))
L_{rad}	luminosity of thermal radiation from the outer surface of the ejected material (cf. Equations (34), (74), and (100))
$L_{rad,in}$	luminosity of thermal radiation from the ejected material radiated toward the interior (Phase II,III; cf. Equations (73) and (101))
$L_{rad,pul}$	luminosity of thermal radiation from the NS surface (Phase II,III; cf. Equation (51))
L_{sd}	spin-down luminosity of the pulsar (Phase II, III; cf. Equation(48))
η_{B_n}	fraction of the total pulsar wind power injected as magnetic energy per unit time into the PWN (cf. Sections 4.2.2 and 4.3.1)
η_{TS}	efficiency of converting pulsar wind power into random kinetic energy of accelerated particles in the PWN (cf. Equations (9), (76) and Sections 4.2.2, 4.3.1)

(e.g., Dessart et al. 2009). This wind can be treated as roughly spherically symmetric at distances $r \gtrsim R_{min} = 30$ km (cf., e.g., Siegel et al. 2014; Siegel & Ciolfi 2015b), which we define as our inner spatial boundary of the evolution model.

Such a magnetically and/or neutrino-induced wind is likely to dominate baryon pollution around the newly-formed NS on the timescales of interest. Dynamical ejecta originating from the tidal tails during the merger process will be ejected mostly into the equatorial plane and move away from the merger site with high (mildly relativistic) velocities (e.g., Davies et al. 1994; Oechslin et al. 2007; Bauswein et al. 2013; Hotokezaka et al. 2013; Rosswog et al. 2013). They are thought to undergo r-process nucleosynthesis and to possibly power a macronova (also known as a kilonova; e.g., Li & Paczyński 1998; Metzger et al. 2010; Barnes & Kasen 2013; Piran et al. 2013; Tanaka & Hotokezaka 2013). The more isotropic dynamical ejection originating from shock heating at the contact interface during collision of the NSs and aided by radial oscillations of the double-core structure of the newly-formed NS immediately after merger (Bauswein et al. 2013; Hotokezaka et al. 2013; Kastaun & Galeazzi 2015) only lasts for a few milliseconds and is thus unlikely to dominate baryon pollution on the much longer timescales relevant here. Such a component can, however, be accounted for in our wind model by, e.g., tuning the mass ejection rate \dot{M} (see below).

4.1.1. Wind Model

In order to avoid performing expensive hydrodynamical simulations, we describe the generation and evolution of the baryon-loaded wind by a simple one-dimensional model. In particular, we assume that there are no hydrodynamical shocks being formed in the wind. The assumption of spherical symmetry is motivated by recent three-dimensional magneto-hydrodynamic simulations in general relativity, which have shown that for the most realistic magnetic field configurations, such a wind will be highly isotropic (Siegel et al. 2014; Siegel & Ciolfi 2015b). Our simple approach is furthermore justified by the fact that the exact details of modeling this wind only have a minor influence on the final predictions of our model, such as the lightcurves, as the pulsar nebula shock eventually sweeps up all the material into a thin shell in Phase II.

It is conceivable to assume that a fluid element of the wind ejected from the NS at time t moves outward with a constant velocity $v(r, t) = v(t)$, once it has climbed up the gravitational potential of the NS after a few tens of kilometers. Mass conservation requires $v(r, t) = \dot{M}(t)/4\pi r^2 \rho(r, t)$, where ρ denotes the rest-mass density and $\dot{M}(t)$ the mass injection rate into the wind. Hence, in order to satisfy $v(r, t) = v(t)$, $\rho(r, t) = A(t)/r^2$ for matter ejected at time t . This assumption is also supported by recent general-relativistic magnetohydrodynamic simulations of magnetically driven winds that yielded a $\rho \propto r^{-2}$ density profile and constant ejection velocities for a

constant \dot{M} over the timescale of tens of milliseconds (Siegel et al. 2014; Siegel & Ciolfi 2015b).

While differential rotation is being removed on a timescale t_{dr} , i.e., the gradient of the angular frequency decays as

$$|\nabla\Omega| \propto \exp(-t/t_{\text{dr}}), \quad (16)$$

we also expect that the mass ejection rate, therefore the density profile, and the ejection speed decay on roughly similar timescales:

$$\dot{M}(t) = \dot{M}_{\text{in}} \exp(-\sigma_M t/t_{\text{dr}}), \quad (17)$$

$$A(t) = A_{\text{in}} \exp(-\sigma_\rho t/t_{\text{dr}}), \quad (18)$$

$$v(t) = v_{\text{ej,in}} \exp(-\sigma_v t/t_{\text{dr}}), \quad (19)$$

where $\sigma_M, \sigma_\rho, \sigma_v$ are of the order of one. This set of assumptions satisfies the “no-shocks-requirement” and immediately yields for the outer radius of the wind:

$$R_{\text{ej}}(t) = R_{\text{min}} + v_{\text{ej,in}} t. \quad (20)$$

Equations (17)–(19) only apply for a magnetically driven wind (Siegel et al. 2014). However, typical values for $t_{\text{dr}} \lesssim 1$ s agree well with typical neutrino cooling timescales, such that a neutrino-driven wind can be additionally incorporated in the model by tuning \dot{M}_{in} . We note that even for moderate magnetic field strengths and realistic rotation periods of the NS the magnetically driven wind can easily exceed mass loss rates of a few in $10^{-3} M_\odot \text{ s}^{-1}$ and thus dominate over the other ejection mechanisms. If the neutrino cooling timescale is very different from t_{dr} the situation could be different. However, as the pulsar wind shock eventually sweeps up all the ejecta material into a thin shell, the following evolution will mostly depend on the total amount of emitted material $M_{\text{ej}} \propto \dot{M}_{\text{in}} t_{\text{dr}}$. Hence, by varying t_{dr} and \dot{M}_{in} the above model for mass ejection can effectively also accommodate a dominant neutrino-induced wind.

Simple scaling arguments can fix two of the free parameters $\sigma_M, \sigma_\rho, \sigma_v$ that control the decay timescales relative to t_{dr} . Magnetic winding in the stellar interior converts rotational energy into magnetic energy (mostly into toroidal field strength) at a rate $\propto |\nabla\Omega|^2$ (e.g., Duez et al. 2006; Siegel et al. 2013). This magnetic energy is then available to be dissipated into kinetic and EM energy of a wind driven by the built-up of magnetic pressure in the stellar interior (Siegel et al. 2014). Consequently,

$$\frac{1}{2} \dot{M} v^2 + L_{\text{EM}} \propto |\nabla\Omega|^2, \quad (21)$$

where L_{EM} denotes the EM luminosity corresponding to the Poynting flux carried by the wind (cf. also Section 4.1.2). From Equations (16) and (21) we conclude that $L_{\text{EM}} \propto \exp(-\sigma_L t/t_{\text{dr}})$, with $\sigma_L = 2$, and

$$\sigma_M + 2\sigma_v = 2. \quad (22)$$

At $r = R_{\text{min}}$, we also need to satisfy $v(t) = \dot{M}(t)/4\pi\rho(R_{\text{min}}, t)R_{\text{min}}^2$. Using Equations (17)–(19), this yields

$$\sigma_M = \sigma_\rho + \sigma_v \quad (23)$$

and $A_{\text{in}} = \dot{M}_{\text{in}}/4\pi v_{\text{ej,in}}$. According to Equations (22) and (23), only one σ -parameter can be chosen independently. The additional requirement of $\sigma_M, \sigma_\rho, \sigma_v$ all being non-negative

limits these parameters to the following ranges:

$$\sigma_M \in [1, 2] \quad (24)$$

$$\sigma_\rho \in [0.5, 2] \quad (25)$$

$$\sigma_v \in [0, 0.5]. \quad (26)$$

In order to compute the density profile $\rho(r, t)$ of the wind resulting from the mass ejection model (17)–(19), we first compute the total mass contained in a volume of radius r at time t ,

$$\begin{aligned} m_w(r, t) &= \int_{\bar{r}(r)}^t \dot{M}(t') dt' \\ &= \frac{t_{\text{dr}}}{\sigma_M} \dot{M}_{\text{in}} \left[\exp\left(-\sigma_M \frac{\bar{r}(r, t)}{t_{\text{dr}}}\right) - \exp\left(-\sigma_M \frac{t}{t_{\text{dr}}}\right) \right], \end{aligned} \quad (27)$$

where $\bar{r}(r, t)$ denotes the time a fluid element at r and t was sent out from the inner boundary at $r = R_{\text{min}}$, i.e., \bar{t} is determined by $r = v(\bar{t})(t - \bar{t}) + R_{\text{min}}$, or, equivalently,

$$(t - \bar{t}) \exp\left(-\sigma_v \frac{\bar{t}}{t_{\text{dr}}}\right) - \frac{r - R_{\text{min}}}{v_{\text{ej,in}}} = 0. \quad (28)$$

It is straightforward to show that Equation (28) has exactly one root in $[0, t]$, such that $\bar{r}(r, t)$ is well defined. At any time t the density profile of the wind is then given by

$$\rho_{w,t}(r) = \frac{1}{4\pi r^2} \frac{\partial m_w(r, t)}{\partial r}. \quad (29)$$

The corresponding velocity profile is

$$v_w(r, t) = v_{\text{ej,in}} \exp\left(-\sigma_v \frac{\bar{r}(r, t)}{t_{\text{dr}}}\right) \quad (30)$$

and the total amount of ejected mass at time t is given by

$$\begin{aligned} M_{\text{ej}}(t) &= m_w(R_{\text{ej}}(t), t) \\ &= \frac{t_{\text{dr}}}{\sigma_M} \dot{M}_{\text{in}} \left[1 - \exp\left(-\sigma_M \frac{t}{t_{\text{dr}}}\right) \right]. \end{aligned} \quad (31)$$

4.1.2. Properties of the Ejected Matter

Injection of electromagnetic energy—The wind will be endowed with a Poynting flux of luminosity (see Siegel et al. 2014 and Section 4.1.1)

$$\begin{aligned} L_{\text{EM}}(t) &\simeq 10^{48} \left(\frac{\bar{B}}{10^{15} \text{ G}} \right)^2 \left(\frac{R_e}{10^6 \text{ cm}} \right)^3 \left(\frac{P_c}{10^{-4} \text{ s}} \right)^{-1} \\ &\quad \times \exp\left(-\sigma_L \frac{t}{t_{\text{dr}}}\right) \text{ erg s}^{-1}, \end{aligned} \quad (32)$$

where $\sigma_L = 2$. While t_{dr} is a free parameter of our model, the total magnetic field strength in the outer layers of the NS, \bar{B} , the equatorial radius R_e , as well as the central spin period P_c of the differentially rotating NS can be extracted from numerical relativity simulations. The wind itself is highly turbulent in the vicinity of the NS (Siegel et al. 2014) and magnetic dissipation will therefore be very effective. We assume that this Poynting flux is dissipated and thermalized in the ejecta matter (due to the very high optical depth) on the timescales of interest, such

that this energy is trapped and thus appears as a source term in Equation (2).

Injection of thermal energy—The material ejected from the NS surface as probed by numerical relativity simulations typically has a very high specific internal energy $\epsilon_{\text{ej,NS,in}}$ that corresponds to a temperature $T_{\text{ej,NS,in}}$ of the order of tens of MeV (e.g., Siegel et al. 2014; Kastaun & Galeazzi 2015). We therefore source the internal energy of the ejected material in Equation (2) by the corresponding injection rate

$$\frac{dE_{\text{th,NS}}}{dt} = \epsilon_{\text{ej,NS,in}} \dot{M}_{\text{in}} \exp\left(-\sigma_M \frac{t}{t_{\text{dr}}} - \frac{t}{t_\nu}\right), \quad (33)$$

where we have assumed that the NS matter cools down due to neutrino cooling on a timescale t_ν .

Thermal radiation from the wind—Due to the very high optical depth of the wind material, the radiation originating from the surface of the expanding wind will be predominantly thermal in Phase I. This leads to radiative losses in Equation (2) with a luminosity

$$L_{\text{rad}}(t) = 4\pi R_{\text{ej}}^2(t) \sigma T_{\text{eff}}^4(t), \quad (34)$$

where σ denotes the Stefan-Boltzmann constant. The effective temperature of the wind, T_{eff} , is given by

$$T_{\text{eff}}^4(t) \simeq \frac{16}{3} \frac{T^4(t)}{\Delta\tau(t) + 1}. \quad (35)$$

Here,

$$\Delta\tau(t) = \kappa \int_{R_{\text{in}}(t)}^{R_{\text{ej}}(t)} \rho_{\text{w},t}(r) dr \quad (36)$$

is the optical depth of the wind with associated diffusion timescale

$$t_{\text{diff}}(t) = \frac{R_{\text{ej}}(t) - R_{\text{in}}(t)}{c} [\Delta\tau(t) + 1]. \quad (37)$$

Adding unity here and in the definition of T_{eff} takes a possible transition to the optically thin regime into account. κ is the opacity of the ejecta material and $R_{\text{in}}(t)$ denotes the effective inner radius of the ejected material, defined by the condition

$$\kappa \int_{R_{\text{min}}}^{R_{\text{in}}(t)} \rho_{\text{w},t}(r) dr = 1. \quad (38)$$

We describe the wind material as a mixture of ideal gas with adiabatic index $\Gamma_{\text{ej}} = 4/3$ and radiation. The temperature $T(t)$ of the wind in Equation (35) at time t is thus obtained as the root of the following equation:

$$T(t)^4 + \frac{1}{\Gamma_{\text{ej}} - 1} \frac{k_B}{m_p a} \bar{\rho}_w(t) T(t) - \frac{E_{\text{th}}(t)}{a V_{\text{ej}}(t)} = 0, \quad (39)$$

where k_B is the Boltzmann constant, m_p denotes the proton mass, a is the radiation constant, $V_{\text{ej}}(t) = (4/3)\pi [R_{\text{ej}}^3(t) - R_{\text{in}}^3(t)]$ the volume of the ejecta material, and $\bar{\rho}_w(t) = [m_w(R_{\text{ej}}(t), t) - m_w(R_{\text{in}}(t), t)]/V_{\text{ej}}(t)$ its mean density.

4.2. Phase II: Pulsar Wind Shock

4.2.1. Pulsar Properties

“Ignition”—As differential rotation is being removed the NS settles down to uniform rotation and mass ejection is suppressed according to the wind model discussed in Section 4.1.1. This eventually creates the conditions to build up a pulsar magnetosphere. As a criterion to “switch on” the pulsar, we employ $\rho(R_{\text{min}}, t) = (A_{\text{in}}/R_{\text{min}}^2) \exp(-\sigma_\rho t/t_{\text{dr}}) < \rho_{\text{crit}}$, which translates into a time

$$t_{\text{pul,in}} = -\frac{t_{\text{dr}}}{\sigma_\rho} \ln\left(\frac{\rho_{\text{crit}} R_{\text{min}}^2}{A_{\text{in}}}\right). \quad (40)$$

For the critical density we typically choose the rest-mass density for Iron ions corresponding to the Goldreich-Julian charge density, $\rho_{\text{crit}} \sim \rho_{\text{GJ}}[\text{Fe}] \sim 6 \times 10^{-6} \text{ g cm}^{-3}$, assuming typical magnetic fields of 10^{15} G and rotational periods of the pulsar of $\sim 1 \text{ ms}$ (Goldreich & Julian 1969). We note, however, that as the density in the vicinity of the NS decreases exponentially, varying the choice of ρ_{crit} even by orders of magnitude does not influence the model evolution noticeably, as long as the value is sufficiently small.

Initial spin and magnetic field—Once the NS has settled down to uniform rotation, it is expected to maintain roughly the same level of magnetization on the timescales of interest. In Phase I, strong toroidal fields have been built up through magnetic winding and possibly instabilities like the magnetorotational instability (Duez et al. 2006; Siegel et al. 2013; Kiuchi et al. 2014; Siegel et al. 2015b), such that the strength of the dipolar component of the poloidal field at the pole B_p is only a fraction η_{B_p} of the total magnetic field strength in the outer layers of the NS,

$$B_p = \eta_{B_p} \bar{B}. \quad (41)$$

This dipole component is the relevant quantity for dipole spin-down emission (see the next paragraph). Knowing the initial rotational energy $E_{\text{rot,NS,in}}$ of the differentially rotating NS from numerical relativity simulations, we can infer the initial spin period of the pulsar $P_{\text{pul,in}}$ at $t_{\text{pul,in}}$ from its initial rotational energy $E_{\text{rot,pul,in}}$:

$$E_{\text{rot,pul,in}} = E_{\text{rot,NS,in}} - E_{\text{EM}} - E_{\text{kin,w}} - E_{\text{rot,ej}}. \quad (42)$$

Here,

$$E_{\text{EM}} = \int_0^{t_{\text{pul,in}}} L_{\text{EM}}(t) dt \quad (43)$$

is the rotational energy dissipated into Poynting flux during Phase I,

$$E_{\text{kin,w}} = \frac{1}{2} 4\pi \int_{R_{\text{min}}}^{R_{\text{ej}}(t_{\text{pul,in}})} \rho_{\text{w},t_{\text{pul,in}}}(r) v_w^2(r, t_{\text{pul,in}}) r^2 dr \quad (44)$$

is the rotational energy dissipated into kinetic energy of the radially expanding wind in Phase I, and

$$E_{\text{rot,ej}} \sim \frac{M_{\text{ej}}(t_{\text{pul,in}})}{M_{\text{NS,in}}} E_{\text{rot,NS,in}} \quad (45)$$

approximates the (subdominant) amount of initial rotational energy carried away by the ejected matter. The initial mass $M_{\text{NS,in}}$ of the NS at birth is known from numerical relativity

simulations. The initial spin period is then given by

$$P_{\text{pul,in}} = 2\pi \left(\frac{2E_{\text{rot,pul,in}}}{I_{\text{pul}}} \right)^{-\frac{1}{2}}, \quad (46)$$

where I_{pul} is the moment of inertia of the pulsar.

Spin-down luminosity—Due to unipolar induction charged particles are continuously extracted from the pulsar surface (Goldreich & Julian 1969). This primary particle current initiates copious pair production, which populates the magnetosphere with a nearly force-free plasma and drives a highly relativistic, magnetized (Poynting-flux dominated) outflow of particles (mostly electrons and positrons), referred to as a pulsar wind. The associated Poynting-flux luminosity is given by (Spitkovsky 2006; Philippov et al. 2015)

$$L_{\text{sd,in}} = \frac{(2\pi)^4 B_p^2 R_{\text{pul}}^6}{4c^3 P_{\text{pul,in}}^4} (k_0 + k_1 \sin^2 \chi), \quad (47)$$

where $k_0 = 1.0 \pm 0.1$, $k_1 = 1.1 \pm 0.1$, χ is the inclination angle of the dipole component of the magnetic field with respect to the rotation axis of the pulsar, and $R_{\text{pul}} \simeq R_e$ denotes the radius of the pulsar. This Poynting flux is extracted from the pulsar via the magnetic field at the expense of rotational energy $E_{\text{rot,pul}}$. Observations of well studied objects like the Crab pulsar suggest that only $\sim 1\%$ of the observed spin-down energy is directly radiated away by the pulsar (Bühler & Blandford 2014), such that essentially the entire spin-down energy is carried by the pulsar wind leaving the light cylinder. Hence, we can set $\dot{E}_{\text{rot,pul}} = L_{\text{sd}}$, which results in slowing down the pulsar spin $P_{\text{pul}}(t) \propto \sqrt{1 + t/t_{\text{sd}}}$ and yields a spin-down luminosity of

$$L_{\text{sd}}(t) = L_{\text{sd,in}} \left(1 + \frac{t - t_{\text{pul,in}}}{t_{\text{sd}}} \right)^{-2}, \quad (48)$$

where

$$t_{\text{sd}} = \frac{E_{\text{rot,pul,in}}}{L_{\text{sd,in}}} \quad (49)$$

is the spin-down timescale. In the following, we assume an aligned rotator, i.e., $\chi = 0$, as a non-zero inclination angle would result in a change of L_{sd} of order unity, which can be absorbed, e.g., in the parameter η_{B_p} that sets the initial field strength B_p (see Equation (41)).

Emission of thermal energy—Immediately after the BNS merger the NS matter is very hot with temperatures of a few tens of MeV. It cools down via neutrino emission on a timescale $t_\nu \lesssim 1$ s. This thermal energy reservoir can be tapped via ejection of material in Phase I (cf. Equation (33)) and by thermal radiation from the pulsar surface in Phase II and III. Thermal radiation from the pulsar can help initiate secondary-particle cascades based on the primary charged particles extracted from the pulsar surface. The associated energy is thus reprocessed in the magnetosphere and will be carried away by the pulsar wind. However, given typical neutrino cooling timescales, this thermal energy contribution will become energetically negligible very soon with respect to, e.g., the spin-down luminosity. Therefore, we adopt a simple cooling

model for the pulsar surface,

$$T_{\text{NS}}(t) = T_{\text{NS,in}} \exp\left(-\frac{t}{t_\nu}\right), \quad (50)$$

with associated thermal radiation of luminosity

$$L_{\text{rad,pul}}(t) = 4\pi R_{\text{pul}}^2 \sigma T_{\text{NS}}^4(t). \quad (51)$$

Here, $T_{\text{NS,in}}$ is the initial typical surface temperature of the NS corresponding to the specific internal energy $\epsilon_{\text{ej,NS,in}}$ (cf. Section 4.1.2). As the thermal energy is reprocessed in the magnetosphere, we add $L_{\text{rad,pul}}$ as a source term to the evolution Equation (9) and as an input for the nebula in Phase III (cf. Section 4.3.1).

4.2.2. Simple Model for the Expanding Pulsar Wind Nebula

The newly-formed pulsar wind (Section 4.2.1) leaves the magnetosphere with relativistic velocities and inflates a PWN behind the less rapidly expanding ejecta material (e.g., Kennel & Coroniti 1984a; see Section 4.3.1 for more details). The PWN is highly overpressured with respect to the surrounding ejecta matter and thus drives a strong hydrodynamical shock into the material (see Section 4.2.3), which, in turn, leads to a rapid expansion of the PWN. The exact physical description of such a highly dynamical PWN is complex. However, the main energetical features that govern the overall dynamics of the system (which is what we are interested in here) can be captured using a simple approach inspired by recent dynamical PWN models (e.g., Gelfand et al. 2009; Kotera et al. 2013; Metzger & Piro 2014; Metzger et al. 2014): we formulate the energetics of the PWN in terms of a balance equation for the total internal energy E_{nth} of the nebula (photons and random kinetic energy of the particles; cf. Equation (9)). The internal energy of the PWN is sourced by the spin-down luminosity L_{sd} (Equation (48)), thermal radiation from the pulsar surface $L_{\text{rad,pul}}$ (Equation (51)) as discussed above (which can represent a significant contribution at early times), and thermal radiation emitted by the hot ejecta matter toward the interior with luminosity $L_{\text{rad,in}}$ (Equation (73)). We assume that only a fraction η_{TS} of the spin-down luminosity and the thermal radiation from the pulsar surface are dissipated into random kinetic energy of the particles in the nebula. This parameter reflects our incomplete knowledge about the efficiency with which the bulk energy of the pulsar wind is dissipated in the nebula (see Section 4.3.1 for more details).

Rapid expansion of the PWN occurs at the expense of $p dV$ work,

$$\frac{dE_{pdV}}{dt} = -p_n \frac{dV_n}{dt} = -\frac{E_{\text{nth}}}{R_n} \frac{dR_n}{dt}, \quad (52)$$

where

$$p_n = \frac{E_{\text{nth}}}{3V_n} + \frac{B_n^2}{8\pi} \quad (53)$$

is the pressure inside the nebula with volume $V_n = (4/3)\pi R_n^3$ and radius R_n . Here we have assumed that the particles inside the nebula are relativistic and collisionless (cf. Section 4.3.1), such that they form an ideal gas with adiabatic index $4/3$. The second pressure contribution on the right hand side of Equation (53) is caused by the uniform and isotropic magnetic field that we assign to the nebula. Its field strength B_n at time t

is inferred from the total magnetic energy

$$E_B = \frac{B_n^2}{8\pi} V_n \quad (54)$$

of the nebula, which we evolve according to Equation (10). The parameter η_{B_n} in Equation (10) controls the level of magnetization of the nebula (see also Section 4.3.1). We note that the efficiency parameters have to satisfy $\eta_{TS} + \eta_{B_n} \leq 1$.

Furthermore, the nebula loses energy through irradiation of the surrounding ejecta matter. The internal energy of the nebula is radiated away on the diffusion timescale through various radiative processes that we do not model in detail in Phase II (see, however, Section 4.3.1). We may write the associated luminosity as $L_{nth}(t) = E_{nth}(t)/t_{diff,n}(t)$, where

$$t_{diff,n}(t) = \frac{R_n(t)}{c} [1 + \Delta\tau_T(t)] \quad (55)$$

is the photon diffusion timescale of the nebula due to Thomson scattering of photons off thermal electrons and positrons. Here,

$$\Delta\tau_T(t) = \sqrt{\frac{4Y\sigma_T L_{sd}(t)}{\pi R_n(t) m_e c^3}} \quad (56)$$

is the optical depth to Thomson scattering, with σ_T the Thomson cross section, m_e the electron mass, and Y the pair yield of the nebula (Lightman & Zdziarski 1987). Given the very high electron compactness parameter $l_e \gg 1$ during Phase II (see Section 4.3.1), the pair yield is given by $Y \simeq 0.1$ (Lightman & Zdziarski 1987; Svensson 1987). We have added the light crossing time in Equation (55) to account for a possible transition to the optically thin regime.

Ionization of ejecta matter due to nebula radiation can cause a non-zero albedo \mathcal{A} , which, in turn, can be frequency dependent, such that the radiative losses of the nebula may be written as (see also Metzger & Piro 2014; Metzger et al. 2014)

$$\frac{dE_{PWN}}{dt} = f_{beam}(t) \int [1 - \mathcal{A}(t, \nu)] L_{nth}(t, \nu) d\nu, \quad (57)$$

with $\int L_{nth}(t, \nu) d\nu = L_{nth}(t)$. Due to relativistic expansion of the PWN with velocity $v_n = dR_n/dt$ (cf. Equation (5)), relativistic beaming will prevent a sizable fraction $1 - f_{beam}$ of photons to escape from the nebula. Therefore, we have additionally included a factor $f_{beam}(t) = 1 - v_n^2(t)/c^2$ in Equation (57). As the radiative losses given by Equation (57) are thermalized in the surrounding ejecta shell, the resulting light curve neither depends on the exact spectral shape of nebula radiation $L_{nth}(t, \nu)$ nor on the spectral shape of $\mathcal{A}(\nu, t)$. Therefore, we typically set $\mathcal{A}(t, \nu) = \mathcal{A}(t)$ and we need not assume a spectral shape for $L_{nth}(t)$.

4.2.3. Shock Dynamics and Ejecta Properties

The high nebula pressure (53) drives a strong hydrodynamic shock into the ejecta matter. The shock front (denoted by the radial coordinate R_{sh}) divides the ejecta matter into shocked ejecta with internal energy $E_{th,sh}$ and unshocked ejecta with internal energy $E_{th,ush}$ (cf. Figure 2). The PWN with radius R_n is separated from the shocked ejecta material by a contact discontinuity. We denote the radial thickness of the shocked ejecta layer by $\Delta_{sh} = R_{sh} - R_n$.

Shock propagation—In order to avoid performing hydrodynamical simulations, we describe the shock dynamics by a simple model (Equations (4) and (5)). According to the special-relativistic Rankine–Hugoniot conditions, the shock speed as measured in the lab frame is given by (see Appendix A.1)

$$v_{sh}(t) = \frac{v_w(R_{sh}(t), t) + v_{sh,R}(t)}{1 + v_w(R_{sh}(t), t)v_{sh,R}(t)/c^2}, \quad (58)$$

where

$$v_{sh,R} = \left\{ \frac{p_n}{\rho_R \left[1 - \frac{\rho_R}{\rho_L} \left(1 + \frac{\Gamma_{ej}}{\Gamma_{ej} - 1} \frac{p_n}{\rho_L c^2} \right) + \frac{p_n}{\rho_R c^2} \right]} \right\}^{\frac{1}{2}} \quad (59)$$

is the shock velocity in the frame comoving with the unshocked fluid. Here, $\rho_R(t) = \rho_{w,t}(R_{sh}(t))$ is the density of the unshocked fluid at the shock front and

$$\rho_L = \frac{\Gamma_{ej} + 1}{\Gamma_{ej} - 1} \rho_R \frac{1}{2} \left\{ 1 + \left[1 + 4 \frac{p_n}{\rho_R c^2} \frac{\Gamma_{ej}}{(\Gamma_{ej} + 1)^2} \right]^{\frac{1}{2}} \right\} \quad (60)$$

is the density of the shocked fluid at the shock front (see Appendix A.1). A special-relativistic framework for shock propagation is required here due to the very low baryon densities in the surrounding of the pulsar (cf. Equation (40)) and the very high pressure of the pulsar nebula (Equation (53)), which result in highly relativistic initial shock propagation speeds. The shock front decelerates as it propagates outward into higher density regions further out from the pulsar and eventually slows down to non-relativistic or mildly relativistic velocities once it reaches the outer surface of the ejecta material. As the shock front is evolved using Equation (4), the thickness Δ_{sh} of the shocked ejecta layer and thus R_n (cf. Equation (5)) is adjusted such that pressure equilibrium between the nebula and the shocked ejecta layer is maintained. For a mixture of ideal gas with $\Gamma_{ej} = 4/3$ and radiation, this results in the following constraint:

$$R_n = R_{sh} \frac{E_{th,sh}}{E_{nth}}. \quad (61)$$

This conditions defines $d\Delta_{sh}/dt$ and couples Equations (5) and (9) to make them implicit evolution Equations for R_n and E_{nth} .

Shock related energetics—The shocked and unshocked ejecta material are assigned internal energies $E_{th,sh}$ and $E_{th,ush}$, respectively, which are evolved separately (cf. Equations (6) and (7)). As the shock propagates across the ejecta matter internal energy is transferred from the unshocked to the shocked fluid part, which amounts to

$$dE_{th,vol} = E_{th,ush} \frac{(R_{sh} + dR_{sh})^3}{R_{ej}^3 - R_{sh}^3} \quad (62)$$

during a time dt . Furthermore, as the fluid is swept up by the shock it is heated at a rate

$$\frac{dE_{sh}}{dt} = \Delta\epsilon \frac{dm_{sh}}{dt}, \quad (63)$$

where

$$\Delta\epsilon = \frac{1}{\Gamma_{\text{ej}} + 1} \frac{p_n}{\rho_R} \frac{2}{1 + \left[1 + \frac{4\Gamma_{\text{ej}}}{(\Gamma_{\text{ej}} + 1)^2} \frac{p_n}{\rho_R c^2} \right]^{\frac{1}{2}}} \quad (64)$$

is the jump in specific internal energy across the shock front (see Appendix A.1) and

$$\frac{dm_{\text{sh}}}{dt} = 4\pi R_{\text{sh}}^2 \rho_R \frac{1}{\sqrt{1 - \frac{v_w^2(R_{\text{sh}}, \cdot)}{c^2}}} [v_{\text{sh}} - v_w(R_{\text{sh}}, \cdot)] \quad (65)$$

is the amount of material swept up by the shock per unit time. The latter expression is obtained by noting that the amount of material in a spherical volume changes by

$$dm = \frac{4\pi r^2 \rho}{\sqrt{1 - \frac{v^2}{c^2}}} dr - \frac{4\pi r^2 \rho v}{\sqrt{1 - \frac{v^2}{c^2}}} dt \quad (66)$$

if the radius of the volume r is altered by dr during a time dt , assuming that the fluid is radially moving outward with velocity v .

For further reference (see Section 4.3.2), we also note that the shock deposits kinetic energy in the shocked ejecta material. The jump Δe_{kin} in specific kinetic energy across the shock front as measured in the lab frame is given by

$$\frac{\Delta e_{\text{kin}}}{c^2} = \left[1 - \left(\frac{v_L^{\text{Lab}}}{c} \right)^2 \right]^{-\frac{1}{2}} - \left[1 - \left(\frac{v_R^{\text{Lab}}}{c} \right)^2 \right]^{-\frac{1}{2}}, \quad (67)$$

where $v_R^{\text{Lab}}(t) = v_w(R_{\text{sh}}(t), t)$ is the velocity of the wind in the unshocked fluid part at the shock front as measured in the lab frame. Furthermore,

$$v_L^{\text{Lab}}(t) = \frac{v_L(t) + v_{\text{sh}}(t)}{1 + v_L(t)v_{\text{sh}}(t)/c^2} \quad (68)$$

is the velocity of the shocked fluid at the shock front as measured in the lab frame, with v_L being the velocity of the shocked fluid at the shock front in the frame comoving with the shock front (see Appendix A.1).

Thermal emission—As in Phase I, we assume that the ejecta matter consists of a mixture of ideal gas and photons. The corresponding fluid temperatures T_{sh} and T_{ush} are given by

$$T_{\text{sh,ush}}^4 + \frac{1}{\Gamma_{\text{ej}} - 1} \frac{k_B}{m_p a} \bar{\rho}_{\text{sh,ush}} T_{\text{sh,ush}} - \frac{E_{\text{th,sh,ush}}}{a V_{\text{sh,ush}}} = 0, \quad (69)$$

where $\bar{\rho}_{\text{sh}}(t) = m_w(R_{\text{sh}}(t), t)/V_{\text{sh}}(t)$ and $\bar{\rho}_{\text{ush}}(t) = [m_w(R_{\text{ej}}(t), t) - m_w(R_{\text{sh}}(t), t)]/V_{\text{ush}}$ are the mean densities of the shocked and unshocked ejecta, respectively, with associated volumes $V_{\text{sh}} = 4\pi(R_{\text{sh}}^3 - R_n^3)/3$ and $V_{\text{ush}} = 4\pi(R_{\text{ej}}^3 - R_{\text{sh}}^3)/3$. The effective temperatures are then defined by

$$T_{\text{eff,sh,ush}}^4(t) \simeq \frac{16}{3} \frac{T_{\text{sh,ush}}^4(t)}{\Delta\tau_{\text{sh,ush}}(t) + 1}, \quad (70)$$

with optical depths

$$\Delta\tau_{\text{sh}}(t) = \kappa \bar{\rho}_{\text{sh}}(t) \Delta_{\text{sh}}(t) \quad (71)$$

and

$$\Delta\tau_{\text{ush}}(t) = \kappa \int_{R_{\text{sh}}(t)}^{R_{\text{ej}}(t)} \rho_{w,t}(r) dr. \quad (72)$$

These effective temperatures give rise to thermal radiation emitted from the inner surface of the shocked ejecta toward the interior with luminosity

$$L_{\text{rad,in}}(t) = 4\pi R_n^2(t) \sigma T_{\text{eff,sh}}^4(t) \quad (73)$$

and from the outer surface of the ejected material with luminosity

$$L_{\text{rad}}(t) = 4\pi R_{\text{ej}}^2(t) \sigma T_{\text{eff,ush}}^4(t). \quad (74)$$

While the radiation associated with L_{rad} leaves the system (cf. Equation (7)), $L_{\text{rad,in}}$ is reabsorbed by the nebula, its energy is reprocessed and eventually reemitted into the ejecta material (cf. Equations (6) and (9)).

Shock break-out—At the time when the shock front reaches the outer ejecta surface a short transient signal can be produced in addition to the thermal radiation from the ejecta. This signal can carry the signature of particle acceleration at the shock front and it can have a non-thermal spectrum reaching higher maximum energies than the background thermal emission; therefore, it could be observable in the hard X-ray and gamma-ray bands. Within the time-reversal scenario (Ciolfi & Siegel 2015b), this transient signal might provide a convincing explanation for the early precursors observed up to $\sim 10^2$ s prior to some SGRBs (Troja et al. 2010).

4.3. Phase III: Pulsar Wind Nebula

Phase III starts at $t_{\text{shock,out}}$, when the shock front reaches the outer surface of the ejecta material, $R_{\text{sh}}(t_{\text{shock,out}}) = R_{\text{ej}}(t_{\text{shock,out}})$. At this time the shock has swept up all the ejecta material of mass $M_{\text{ej}} \equiv M_{\text{ej}}(t_{\text{pul,in}})$ into a thin shell of thickness $\Delta_{\text{ej}} = \Delta_{\text{sh}}(t_{\text{shock,out}})$ (cf. Figure 2), which we assume to be constant during the following evolution. Therefore, we set $dR_n/dt = dR_{\text{ej}}/dt$ for the evolution of the PWN radius R_n in Phase III (cf. Equation (13)). The following two subsections detail the physical description of the PWN and the ejecta shell in this phase.

4.3.1. Physics of the Pulsar Wind Nebula

Basic picture and assumptions—PWNe are traditionally studied in the context of supernovae-born pulsars (see Gaensler & Slane 2006; Bühler & Blandford 2014, and Kargaltsev et al. 2015 for reviews). Only very recently, PWNe have also been considered in the BNS merger scenario (Bucciantini et al. 2012; Metzger & Piro 2014). We study such a system here motivated by the fact that long-lived NSs turn out to be very likely outcomes of BNS mergers (cf. Section 1) and by the fact that the baryonic ejecta (cf. Section 4.1) naturally provide the conditions for such a nebula to form (such as providing the necessary confining envelope). Although the exact physical conditions for a PWN in a BNS merger scenario are different from those in a supernova event, it is conceivable that qualitatively similar morphologies and dynamics emerge. For Phase III, we develop a physical description for a PWN in the context of BNS mergers inspired by studies of supernovae and radiative processes in active galactic nuclei. While spectra of ordinary PWNe from radio to gamma-ray energies can be

explained in terms of synchrotron and inverse Compton emission (for the best studied case, the Crab Nebula, see, e.g., Kennel & Coroniti 1984b; Atoyan & Aharonian 1996; Volpi et al. 2008; Olmi et al. 2014; Porth et al. 2014), the BNS merger scenario requires a more detailed treatment of radiative processes due to the presence of the strong photon field from the confining hot ejecta material. In order to achieve this and in order to avoid performing expensive MHD simulations, we neglect spatial variations and adopt a “one-zone” model for the PWN, in which the nebula is considered to be homogeneous and isotropic. The resulting description of a PWN we propose for Phase III is much more detailed than in Phase II for two reasons. First, Phase III is less dynamical and a quasi-stationary description of the PWN can be adopted that facilitates a detailed treatment of radiative processes. Second, as the ejecta material surrounding the PWN becomes transparent to the nebula radiation at some point, radiation from the nebula itself is not reprocessed and thermalized anymore and its spectrum becomes directly observable. We therefore employ a formalism that predicts the nebula spectrum in a self-consistent way.

The newly formed pulsar loses rotational energy at a rate L_{sd} given by Equation (48) through a highly relativistic magnetized particle outflow, referred to as a pulsar wind (cf. Section 4.2.1). As in Phase II (cf. Section 4.2.2), we also assume that thermal radiation from the pulsar surface with luminosity $L_{\text{rad,pul}}$ (cf. Equation (51)) is deposited in this pulsar wind; this can represent a significant energy contribution at early times when the NS is still very hot. The pulsar wind inflates a PWN behind the less rapidly expanding ejecta material, a bubble of radiation and charged particles (mainly electrons and positrons), which is separated from the pulsar wind by a termination shock at a distance (Gaensler & Slane 2006)

$$R_{\text{TS}} = \sqrt{\frac{L_{\text{sd}}}{4\pi\xi c p_n}} \ll R_n \quad (75)$$

from the pulsar, where the ram pressure of the pulsar wind equals the intrinsic pressure p_n of the nebula; ξ denotes the fraction of a sphere covered by the wind.

Magnetosphere models predict that the pulsar wind leaving the magnetosphere at the light cylinder $R_{\text{LC}} = cP_{\text{pul}}/2\pi$ is highly magnetized, $\sigma_m \gg 1$ (e.g., Arons 2012). Here, σ_m denotes the magnetization parameter, defined as the ratio of Poynting flux to particle energy flux (e.g., Kennel & Coroniti 1984a). One-dimensional and two-dimensional axisymmetric MHD models only reproduce the observed properties of the Crab nebula well if $\sigma_m \ll 1$ just upstream of the termination shock (e.g., Kennel & Coroniti 1984a, 1984b; Atoyan & Aharonian 1996; Volpi et al. 2008; Olmi et al. 2014). Dissipating the Poynting flux into kinetic energy of the particle flow between the light cylinder and the wind termination shock is known as the σ -problem. Recent three-dimensional MHD simulations, however, suggest a solution the σ -problem (Mizuno et al. 2011; Porth et al. 2014). The simulations by Porth et al. (2014) are able to reproduce the morphology of the Crab Nebula even for stronger magnetizations of up to $\sigma_m \simeq \text{few}$, thanks to magnetic dissipation inside the PWN. Enhanced turbulence downstream of the termination shock in the 3D simulations efficiently dissipates magnetic energy, such that the magnetic energy of the nebula is only a very small fraction of the internal energy despite a high magnetization of the pulsar wind at the termination shock. This is in agreement with previous observations and spectral modeling that infer the

magnetic energy of the Crab Nebula to be less than $\approx 3\%$ of the total energy budget (Bühler & Blandford 2014, Porth et al. 2014, and references therein). In our model of the PWN, we control the level of magnetization of the nebula by introducing a factor η_{B_n} , which specifies the amount of inflowing magnetic energy per time in terms of the total power of the pulsar wind: $\dot{E}_B = \eta_{B_n} [L_{\text{sd}}(t) + L_{\text{rad,pul}}(t)]$ (cf. Equations (10) and (15)). The magnetic energy E_B then defines an average magnetic field strength B_n of the nebula through Equation (54).

At the wind termination shock the wind plasma is decelerated and heated, and efficient conversion of flow energy into particle acceleration is thought to take place. The accelerated particles, which are characterized by non-thermal energy spectra, are then advected with the flow while cooling down due to synchrotron emission. Observations of the Crab Nebula synchrotron emission indicate that the conversion of pulsar wind energy into accelerated particles is $\gtrsim 10\%$ (Kennel & Coroniti 1984a; Bühler & Blandford 2014; Olmi et al. 2015; we henceforth denote this efficiency by η_{TS}). While diffusive shock acceleration at the termination shock is now thought to be rather unlikely to occur in the Crab Nebula and other PWNe (Arons 2012; Bühler & Blandford 2014), enhanced turbulence and magnetic dissipation downstream of the termination shock (as found in recent 3D MHD simulations) might provide the required non-thermal particle acceleration site. While the processes of particle acceleration still remain unclear, assuming that the pulsar wind consists of electrons and positrons, and that these particles are reaccelerated into a power-law spectrum at the termination shock, 1D, 2D, and 3D MHD models of the Crab Nebula have been able to reproduce the observed photon spectra very well (Kennel & Coroniti 1984b; Atoyan & Aharonian 1996; Volpi et al. 2008; Camus et al. 2009; Olmi et al. 2014, 2015; Porth et al. 2014).

Following this approach we consider a pulsar wind consisting of electrons and positrons and assume that these particles are injected into the nebula with a power-law spectrum, although more complex injection spectra can easily be accommodated by our model. In view of our “one-zone” description of the nebula, we assume that electrons and positrons are continuously injected uniformly throughout the nebula, instead of being injected at the termination shock and then being advected with the flow. We specify the injection of particles by the following dimensionless compactness parameter (in analogy to Guilbert et al. 1983; Lightman & Zdziarski 1987; Svensson 1987):

$$\begin{aligned} l_e(t) &\equiv \frac{\sigma_{\text{T}}}{m_e c^3 R_n(t)} \eta_{\text{TS}} [L_{\text{sd}}(t) + L_{\text{rad,pul}}(t)] \\ &= \frac{4\pi\sigma_{\text{T}} R_n^2(t)}{3c} \int_1^{\gamma_{\text{max}}} Q(\gamma, t) (\gamma - 1) d\gamma, \end{aligned} \quad (76)$$

where $Q(\gamma, t) = Q_0(t)\gamma^{-\Gamma_e}$ is the number of particles injected per unit time per unit normalized energy $\gamma = \epsilon/m_e c^2$, where ϵ denotes the particle energy, and per unit volume of the nebula. The parameter η_{TS} defines the aforementioned efficiency of converting pulsar wind power into random kinetic energy of accelerated particles. The power-law injection parameters η_{TS} , γ_{max} , and Γ_e are model input parameters, which, in the case of observed PWNe such as the Crab, are usually determined by comparing simulated emission with observational data.

In contrast to ordinary PWNe, where intrinsic photon sources inherent to the pulsar-nebula system are absent and only background photons from the cosmic microwave background (CMB) and potentially from local dust and starlight are “injected” into the nebula, we need to take additional photon sources into account in our description of the PWN that generate a strong photon field. The hot shock-heated ejecta matter confining the PWN injects thermal photons with luminosity $L_{\text{rad,in}}$ (cf. Section 4.3.2, Equation (101)). For completeness, we also include a thermal input spectrum L_{CMB} from the CMB (see below), once the ejecta shell has become optically thin. We specify the resulting photon injection into the nebula in terms of the following dimensionless compactness parameter (in analogy to Lightman & Zdziarski 1987):

$$l_{\text{ph}}(t) \equiv \frac{\sigma_{\text{T}}}{m_e c^3 R_n(t)} [L_{\text{rad,in}}(t) + f_{\text{ej}}(t) L_{\text{CMB}}(t)] \\ = \frac{4\pi\sigma_{\text{T}} R_n^2(t)}{3c} \int_{x_{\text{min}}}^{x_{\text{max}}} \dot{n}_0(x, t) x dx, \quad (77)$$

where \dot{n}_0 denotes the combined number of photons injected per unit time per unit dimensionless energy $x = h\nu/m_e c^2$ per unit volume of the PWN by the aforementioned sources (cf. Equation (80)). Here, h denotes the Planck constant and ν is the photon frequency. Photon energies are assumed to range between x_{min} and x_{max} , which we define in Section 5.2. The function f_{ej} is designed to “switch on” the (subdominant) CMB contribution once the ejecta material becomes optically thin (cf. Equation (102)).

Radiative processes in the PWN reprocess the injected particles and photons and determine the radiative losses of the nebula that are transferred to the surrounding ejecta (denoted by dE_{PWN}/dt in Equation (14)) and the associated emergent spectrum. In particular, they determine how spin-down energy of the pulsar is transmitted to the ejecta material to be radiated away from the system eventually. In contrast to ordinary PWNe, the photon field in our case is typically very strong, such that, expressed in terms of the compactness parameters defined above, l_{ph} can become comparable to l_e or even larger. The photon and particle spectra inside the nebula thus become highly coupled and the computations become intrinsically non-linear. In order to determine those spectra in a self-consistent way under the combined effects of synchrotron losses, (inverse) Compton scattering off thermal and non-thermal particles, pair production and annihilation, and photon escape, we employ, extend and modify a formalism developed for pair plasmas in compact sources such as active galactic nuclei (Lightman & Zdziarski 1987).

Balance equations—Given the setup described above, the physical processes determining the PWN properties and emergent spectra are remarkably similar to those in pair plasmas of active galactic nuclei. Theoretical models to compute detailed emergent spectra for active galactic nuclei have been developed by many authors in the past (e.g., Lightman & Zdziarski 1987; Coppi 1992; Belmont et al. 2008). Consistent with our assumptions, we adopt the approach of Lightman & Zdziarski (1987, henceforth LZ87), but extend and modify it to, e.g., include synchrotron losses. We shall briefly outline the formulation of the equations here with emphasis on the modifications and refer the reader to LZ87 for more details on all other aspects.

According to our “one-zone” model we assume that particles and photons are uniformly injected throughout the spherical volume of the PWN with radius R_n and associated compactness parameters l_e and l_{ph} (Equations (76) and (77)). At a time t and assuming quasi-stationarity, the number densities per unit energy of photons, $n(x)$, and non-thermal particles, $N(\gamma)$, are determined by the following set of highly non-linear, coupled integro-differential equations:

$$0 = \dot{n}_0 + \dot{n}_A + \dot{n}_C^{\text{NT}} + \dot{n}_C^{\text{T}} + \dot{n}_{\text{syn}} \\ - \frac{c}{R_n} n(\Delta\tau_C^{\text{NT}} + \Delta\tau_{\gamma\gamma}) - \dot{n}_{\text{esc}}, \quad (78)$$

$$0 = Q(\gamma) + P(\gamma) + \dot{N}_{\text{C,syn}}(\gamma). \quad (79)$$

Photons at energy x are produced at rates \dot{n}_0 , \dot{n}_A , \dot{n}_C^{NT} , \dot{n}_C^{T} , and \dot{n}_{syn} via injection (cf. Equation (80)), e^{\pm} -pair annihilation, Compton scattering off non-thermal electrons and positrons (cf. Equation (9) in LZ87), Compton scattering off thermal electrons (cf. Equations (22) and (23) in LZ87; see below), and synchrotron cooling of particles (cf. Equation (87)), respectively. For the pair annihilation term \dot{n}_A we use Equations (7), (7) (11), (15)–(18) of Svensson (1983). Photons at energy x are lost due to Compton scattering off non-thermal particles with optical depth $\Delta\tau_C^{\text{NT}}$ (cf. Equation (10) in LZ87), due to e^{\pm} -pair creation with optical depth $\Delta\tau_{\gamma\gamma}$ (cf. Equation (11) in LZ87), and by escaping from the nebula at a rate \dot{n}_{esc} (see Equation (21) of LZ87). Additionally, photons at energy x are lost via Compton scattering off thermal particles (see below), which is accounted for in \dot{n}_C^{T} . Photons not “absorbed” by one of these processes are still impeded from escaping the nebula by Thomson scattering off thermal particles (see below) with scattering depth $\Delta\tau_{\text{T}}$ (cf. Equation (20) in LZ87).

The rate of change of particles at Lorentz factor γ is given by injection into the nebula Q (cf. Equation (76)), e^{\pm} -pair creation P (cf. Equation (13) in LZ87), and non-thermal Compton scattering and synchrotron losses, which are denoted by $\dot{N}_{\text{C,syn}}$ (see below). Particles do not escape from the nebula, i.e., they are assumed to be trapped, e.g., by the magnetic field B_n of the nebula. Once cooled down to $\gamma \sim 1$ and before annihilating, particles are assumed to thermalize and to form a distinct thermal population described by a Maxwell-Boltzmann distribution with dimensionless temperature $\theta_e \equiv k_B T_e/m_e c^2 \ll 1$. The number density of this thermal population is determined in terms of the solution to Equations (78) and (79) by the requirement that pairs must be destroyed at the same rate as they are created in steady state (cf. Equation (18) in LZ87). The temperature of this population can be determined self-consistently by not allowing any net energy transfer between particles and photons via thermal Compton scattering (cf. Equations (27) and (28) in LZ87).

In our implementation, the photon injection term is written as

$$\dot{n}_0 = \dot{n}_{0,\text{ej}} + f_{\text{ej}} \dot{n}_{0,\text{CMB}}, \quad (80)$$

where

$$\dot{n}_{0,\text{ej}}(x, t) = \frac{6\pi}{R_n(t)} \frac{m_e^3 c^4}{h^3} \frac{x^2}{\exp\left(\frac{x m_e c^2}{k_B T_{\text{eff}}(t)}\right) - 1} \quad (81)$$

represents the injection of thermal photons from the ejecta material with effective temperature $T_{\text{eff}} = T_{\text{eff,com}}/(\zeta\gamma_{\text{ej}})^{1/4}$ (cf. Section 4.3.2). The thermal spectrum $\dot{n}_{0,\text{CMB}}$ of the CMB is defined in the same way with an effective temperature of $T_{\text{eff,CMB}} = 2.725$ K and it is “switched on” by the function f_{ej} once the ejecta material becomes optically thin (cf. Equation (102)).

In contrast to LZ87, we additionally include effects of synchrotron radiation (as do Coppi 1992 and Belmont et al. 2008). Here, we briefly outline the way we include those effects via the terms $\dot{N}_{\text{C,syn}}$ and \dot{n}_{syn} . In deriving Equation (79), we assumed that the particle distribution $N(\gamma)$ can be described by the continuity equation

$$\frac{\partial N}{\partial t} + \frac{\partial}{\partial \gamma}(\dot{\gamma}N) = P(\gamma) + Q(\gamma), \quad (82)$$

with $\partial N/\partial t = 0$ in steady state and thus $\dot{N}_{\text{C,syn}} = -\partial(\dot{\gamma}N)/\partial \gamma$. Equation (82) is an accurate description in the case of synchrotron emission and Compton scattering excluding the Klein–Nishina limit (as assumed here for simplicity; Blumenthal & Gould 1970). Assuming steady state, Equation (82) can be integrated to give

$$N(\gamma) = -\dot{\gamma}_{\text{C,syn}}^{-1}(\gamma) \int_{\gamma}^{\gamma_{\text{max}}} [P(\gamma') + Q(\gamma')] d\gamma', \quad (83)$$

where

$$\dot{\gamma}_{\text{C,syn}}(\gamma) = \dot{\gamma}_{\text{C}}(\gamma) + \dot{\gamma}_{\text{syn}}(\gamma) \quad (84)$$

is the combined particle cooling rate due to Compton scattering (excluding the Klein–Nishina limit) and synchrotron emission, with

$$\dot{\gamma}_{\text{C}}(\gamma) = -\sigma_{\text{T}}c \left(\frac{4}{3}\gamma^2 - 1 \right) \int_0^{3/4\gamma} n(x)x dx \quad (85)$$

(cf. Equation (7) in LZ87) and

$$\dot{\gamma}_{\text{syn}}(\gamma) = -\frac{\sqrt{3}e^3B_{\text{n}}}{hm_{\text{e}}c^2} \int_{x_{\text{min}}}^{x_{\text{max}}} \mathcal{R}(x/x_{\text{c}}) dx \quad (86)$$

(cf. Appendix A.3, Equation (172)). The synchrotron losses (86) result in a photon source term

$$\dot{n}_{\text{syn}}(x) = \frac{\sqrt{3}e^3B_{\text{n}}}{hm_{\text{e}}c^2} \frac{1}{x} \int_1^{\gamma_{\text{max}}} N(\gamma)\mathcal{R}(x/x_{\text{c}}) d\gamma \quad (87)$$

(cf. Appendix A.3, Equation (173)). We note that for the stationarity assumption leading to Equation (83) to hold in our evolution scheme (Equations (11)–(15)), the timescale for equilibration of the particle distribution given by the total cooling timescale $|\gamma/\dot{\gamma}_{\text{C,syn}}|$ has to be much smaller than any other evolution timescale for all energies γ . We therefore monitor this quantity to check the validity of the stationarity assumption during the numerical evolution (see Section 5.4). Finally, we note that effects of synchrotron self-absorption have not been considered so far and that they can be neglected for our purposes. In order to check the validity of this assumption, we monitor the optical depth to synchrotron self-

absorption, which can be approximated by

$$\Delta\tau_{\text{syn}}(x) = \frac{\sqrt{3}e^3h^2B_{\text{n}}R_{\text{n}}}{8\pi m_{\text{e}}^4c^6} \frac{1}{x^2} \times \int_1^{\gamma_{\text{max}}} N(\gamma) \left[\frac{\partial}{\partial \gamma} \mathcal{R}(x/x_{\text{c}}) + f(\gamma)\mathcal{R}(x/x_{\text{c}}) \right] d\gamma \quad (88)$$

(cf. Appendix A.3, Equation (175)). Typically, the nebula is optically thin to synchrotron self-absorption at energies of interest (see Section 5.5).

Solving the coupled set of Equations (78) and (79) numerically at time t yields a self-consistent set of spectra $\{n(x), N(\gamma), \dot{n}_{\text{A}}(x), \dot{n}_{\text{C}}^{\text{NT}}(x), \dot{n}_{\text{C}}^{\text{T}}(x), \dot{n}_{\text{syn}}(x), \Delta\tau_{\text{C}}^{\text{NT}}(x), \Delta\tau_{\text{syn}}(x), \Delta\tau_{\text{T}}, \dot{n}_{\text{esc}}(x), P(\gamma), \dot{N}_{\text{C,syn}}(\gamma)\}$. It is important to point out that with the modifications described above, these equations still conserve energy (see Appendix A.4).

The internal energy E_{nth} of the nebula in terms of the solution to Equations (78) and (79) can be written as

$$E_{\text{nth}}(t) = \frac{4}{3}\pi R_{\text{n}}(t)^3 m_{\text{e}}c^2 \left[\int_{x_{\text{min}}}^{x_{\text{max}}} n(x,t)x dx + \int_1^{\gamma_{\text{max}}} N(\gamma)(\gamma-1)d\gamma \right], \quad (89)$$

which is typically dominated by the photon contribution (first term on the right-hand side). The pressure of the nebula is then given by (cf. also Equation (53))

$$p_{\text{n}}(t) = \frac{E_{\text{nth}}(t)}{4\pi R_{\text{n}}^3(t)} + \frac{B_{\text{n}}^2}{8\pi}. \quad (90)$$

Moreover, the luminosity of escaping radiation from the nebula is given by

$$L_{\text{PWN}}(x,t) = \frac{4}{3}\pi R_{\text{n}}(t)^3 m_{\text{e}}c^2 \dot{n}_{\text{esc}}(x,t)x, \quad (91)$$

and thus we arrive at the desired expression for the PWN source term in Equation (14):

$$\frac{dE_{\text{PWN}}}{dt} \equiv L_{\text{PWN}}(t) = \int_{x_{\text{min}}}^{x_{\text{max}}} L_{\text{PWN}}(x,t) dx. \quad (92)$$

4.3.2. Ejecta Properties and Emergent Radiation

Shell kinematics—The initial speed $v_{\text{ej}}(t_{\text{shock,out}})$ of the ejecta shell in Phase III is inferred from its kinetic energy E_{kin} at $t_{\text{shock,out}}$:

$$v_{\text{ej}}(t_{\text{shock,out}}) = c \left[1 - \left(1 + \frac{E_{\text{kin}}(t_{\text{shock,out}})}{M_{\text{ej}}c^2} \right)^{-2} \right]^{\frac{1}{2}}. \quad (93)$$

The total kinetic energy $E_{\text{kin}}(t_{\text{shock,out}}) = E_{\text{kin,w}} + E_{\text{sh,tot}}$ of the ejecta matter is the sum of the kinetic energy of the original wind material $E_{\text{kin,w}}$ (cf. Equation (44)) and the total amount of kinetic energy deposited into the shocked material by the shock,

$$E_{\text{sh,tot}} = \int_{t_{\text{pul,in}}}^{t_{\text{shock,out}}} \Delta e_{\text{kin}} \frac{dm_{\text{sh}}}{dt} dt \quad (94)$$

(cf. Equations (65) and (67)). For typical sub-relativistic or at most mildly relativistic speeds $v_{\text{ej, in}}$ of the outer ejecta front in Phase I and II (cf. Equation (20)), the initial speed of the ejecta shell in Phase III is also at most mildly relativistic.

However, further acceleration according to (cf. Appendix A.2; Equation (11))

$$\frac{dv_{\text{ej}}}{dt} = \gamma_{\text{ej}}^{-3}(t) \alpha_{\text{ej}}(t) \equiv a_{\text{ej}}(t) \quad (95)$$

can be significant if the nebula pressure p_n (Equation (90)) is high. Here, $\gamma_{\text{ej}} = (1 - v_{\text{ej}}^2/c^2)^{-1/2}$ denotes the Lorentz factor of the ejecta shell and $\alpha_{\text{ej}} = 4\pi R_n^2 p_n / M_{\text{ej}}$ is the acceleration of the ejecta shell in the frame comoving with the shell. In order to define a comoving frame we employ the fact that such a freely expanding, spherically symmetric shell at a time t can be described as a thin ring of finite extent in a Milne universe. The transformation between comoving and lab frame is thus achieved via the Milne universe metric. For further details, we refer to Appendix A.2.

Thermal emission—As in Phase I and II, the ejecta matter consists of a mixture of photons and ideal gas with adiabatic index $\Gamma_{\text{ej}} = 4/3$, the temperature of which in the comoving frame, T_{com} , can be found by solving

$$T_{\text{com}}^4 + \frac{1}{\Gamma_{\text{ej}} - 1} \frac{k_B}{m_p a} \rho_{\text{ej}} T_{\text{com}} - \frac{E_{\text{th}}}{a V_{\text{ej}}} = 0. \quad (96)$$

Henceforth q_{com} refers to the value of a quantity q as measured in the frame comoving with the ejecta shell. In Equation (96) we have used the fact that $E_{\text{th}}/V_{\text{ej}} = E_{\text{th, com}}/V_{\text{ej, com}}$ (cf. Appendix A.2). Furthermore, $\rho_{\text{ej}} = M_{\text{ej}}/V_{\text{ej, com}} = M_{\text{ej}}/\zeta V_{\text{ej}}$ is the density of the ejecta shell, where $V_{\text{ej}} = (4/3)\pi(R_{\text{ej}}^3 - R_n^3)$ is its volume in the lab frame and

$$\zeta = \frac{3}{2} \frac{\gamma_{\text{ej}}^2 \beta_{\text{ej}} - \text{arctanh} \beta_{\text{ej}}}{\gamma_{\text{ej}}^3 \beta_{\text{ej}}^3}, \quad (97)$$

with $\beta_{\text{ej}} = v_{\text{ej}}/c$ (cf. Appendix A.2). The associated effective temperature in the comoving frame is given by

$$T_{\text{eff, com}}^4(t) \simeq \frac{16}{3} \frac{T_{\text{com}}^4(t)}{\Delta\tau_{\text{ej, com}}(t) + 1}, \quad (98)$$

where

$$\Delta\tau_{\text{ej, com}}(t) = \kappa \rho_{\text{ej}}(t) \Delta_{\text{ej}}(t) \gamma_{\text{ej}}(t), \quad (99)$$

which gives rise to thermal emission from the outer and inner surface of the ejecta shell with luminosities

$$L_{\text{rad}}(t) = 4\pi R_{\text{ej}}^2(t) \frac{f_{\text{beam}}(t)}{\zeta(t) \gamma_{\text{ej}}(t)} \sigma T_{\text{eff, com}}^4(t) \quad (100)$$

and

$$L_{\text{rad, in}}(t) = 4\pi R_n^2(t) \frac{1}{\zeta(t) \gamma_{\text{ej}}(t)} \sigma T_{\text{eff, com}}^4(t), \quad (101)$$

respectively (cf. Appendix A.2; Equation (14)). In Equation (100), we have again included a factor $f_{\text{beam}} = 1 - v_{\text{ej}}^2/c^2$ to account for relativistic beaming (cf. also Section 4.3.1). This concludes the discussion of source terms in the main evolution Equations (1)–(15) of our model.

4.3.3. Transition to the Optically Thin Regime

Once $\Delta\tau_{\text{ej, com}}$ (cf. Equation (99)) approaches unity, the ejecta material becomes transparent to radiation from the nebula. This non-thermal radiation is not absorbed by the ejecta material anymore and becomes directly observable. In order to ensure a smooth transition between the optically thick and thin regimes, we employ an auxiliary function

$$f_{\text{ej}}(t) = \begin{cases} 0 & \text{if } \Delta\tau_{\text{ej}}(t) > \Delta\tau_{\text{ej, thres}} \\ 1 - \left(\frac{\Delta\tau_{\text{ej}}(t)}{\Delta\tau_{\text{ej, thres}}} \right)^b & \text{if } \Delta\tau_{\text{ej}}(t) \leq \Delta\tau_{\text{ej, thres}} \end{cases} \quad (102)$$

to gradually “switch on or off” terms in the evolution equations during this transition. Here,

$$\Delta\tau_{\text{ej}} = \Delta\tau_{\text{ej, com}} \sqrt{\frac{1 - v_{\text{ej}}/c}{1 + v_{\text{ej}}/c}} \quad (103)$$

approximates the optical depth of the ejecta material as seen from the lab frame (cf. Abramowicz et al. 1991), with $\Delta\tau_{\text{ej, com}}$ defined in Equation (99). We note that this transition function and its parameters b and $\Delta\tau_{\text{ej, thres}}$ are somewhat arbitrary and chosen in such a way that they do not influence the numerical evolution significantly other than guaranteeing a smooth transition from the optically thick to the optically thin regime. Typically, $\Delta\tau_{\text{ej, thres}} \simeq \text{few}$ and $b > 1$.

In particular, as the ejecta material does not absorb nebula radiation anymore, the source term dE_{PWN}/dt (cf. Equation (92)) needs to be removed from the corresponding evolution equation (cf. Equation (14)). Instead, the non-thermal emission from the nebula

$$L_{\text{rad, nth}}(t) = f_{\text{ej}}(t) \frac{dE_{\text{PWN}}}{dt} \quad (104)$$

and its associated spectrum given by Equation (91) become directly observable. Consequently, the ejecta matter also becomes optically thin to photons from the CMB, which are now able to diffuse into the nebula (cf. Equations (77) and (80)).

4.4. Collapse to a Black Hole

Our model applies to hypermassive, supramassive, and stable remnant NSs. If the NS is hypermassive at birth, the expected lifetime is of the order of $t_{\text{dr}} \lesssim 1$ s, unless it migrates to the supramassive regime through substantial mass ejection on shorter timescales. If the NS is supramassive, it can survive on much longer spin-down timescales, although (magneto-) hydrodynamic instabilities can cause an earlier collapse to a black hole. In our model, the time of collapse $t = t_{\text{coll}}$ to a black hole is an input parameter that can be adjusted to cover all possible scenarios.

If the NS collapses to a black hole during Phase I, we keep evolving Equations (1) and (2), setting L_{EM} and $dE_{\text{th, NS}}/dt$ to zero. As the collapse proceeds on the dynamical timescale, which is of the order of milliseconds, we consider the NS collapse at $t \sim t_{\text{dr}} \lesssim 1$ s to be instantaneous as far as the numerical evolution is concerned. The time of collapse is parametrized by $f_{\text{coll, PI}}$ in units of t_{dr} , $t_{\text{coll}} = f_{\text{coll, PI}} t_{\text{dr}}$. We also note that the wind model (cf. Section 4.1.1) has to be adjusted by setting $\dot{M}(t')$ to zero for $t' > t_{\text{coll}}$ in Equation (27). The

resulting EM emission from the system will be predominantly thermal and it will reflect the gradual depletion of the energy reservoir of the ejecta material acquired up to the time of collapse (see also Paper II).

In what follows, we consider a collapse occurring in Phase III.⁴ In the case that the observed prompt γ -ray emission of a SGRB is associated to this collapse as in the recently proposed time-reversal scenario (Ciolfi & Siegel 2015a, 2015b), the resulting lightcurves and spectra of our model after $t = t_{\text{coll}}$ correspond to the observed afterglow radiation of the SGRB.

We parametrize t_{coll} in terms of the spin-down timescale $t_{\text{coll}} = f_{\text{coll}} t_{\text{sd}}$. Scenarios for a wide range of values for f_{coll} are explored in the companion paper (Paper II). The collapse of the NS proceeds on the dynamical timescale, which is of the order of milliseconds and it can thus be considered instantaneous at times $t_{\text{coll}} > t_{\text{pul,in}} \gtrsim 1$ s. At times $t \lesssim \text{few} \times t_{\text{sd}}$, the typical cooling timescales $|\gamma/\dot{\gamma}_{\text{C,syn}}|$ of the non-thermal particles in the nebula (cf. Equation (84)) are orders of magnitude smaller than any other evolution timescale of our model thanks to the relatively strong magnetic field (cf. Equation (86); see also Section 5.4 and Section 4.2 of Paper II). Furthermore, due to this efficient cooling their total number density $N_{\text{tot}} = \int N(\gamma, t) d\gamma \ll N_{\text{th,tot}}$ is orders of magnitude smaller than the total number density $N_{\text{th,tot}}$ of thermalized particles in the nebula. We can therefore assume that the non-thermal particle population is instantaneously thermalized at $t = t_{\text{coll}}$. Furthermore, noting that the optical depth to Thomson scattering $\Delta\tau_{\text{T}}$ is given by $\Delta\tau_{\text{T}} = \sigma_{\text{T}} R_{\text{n}} N_{\text{th,tot}}$, we can conclude that $\Delta\tau_{\text{T}}$ is not affected by this instantaneous thermalization. Pair annihilation becomes increasingly unlikely as the nebula further expands, and can partially be compensated by pair creation induced by photons in the high energy tail of the photon spectrum above the pair creation threshold. As a consequence, the total number of particles is roughly conserved, and the evolution of the Thomson scattering depth for $t > t_{\text{coll}}$ is approximately given by

$$\Delta\tau_{\text{T}}(t) = \Delta\tau_{\text{T}}(t_{\text{coll}}) \left[\frac{R_{\text{n}}(t_{\text{coll}})}{R_{\text{n}}(t)} \right]^2. \quad (105)$$

Due to efficient particle cooling prior to $t = t_{\text{coll}}$ (see above), the energy budget of those photons above the pair creation threshold is typically orders of magnitude smaller than the combined photon energy below the pair creation threshold at t_{coll} . Furthermore, we expect photons to interact with particles mostly via Thomson scattering, as photons that could Compton-scatter off thermal particles are small in number. Noting that Thomson scattering is elastic, we can deduce that for our purposes, the spectral shape of the non-thermal photon spectrum at $t = t_{\text{coll}}$ remains frozen thereafter as photons diffuse out of the nebula on the diffusion timescale

$$t_{\text{diff,n}}(t) = \frac{R_{\text{n}}}{c} [1 + \Delta\tau_{\text{T}}(t)]. \quad (106)$$

Here, we have again added the light crossing time of the nebula to account for a transition to the optically thin regime. The luminosity of the photons diffusing out of the nebula is

⁴ Here we do not discuss the possibility of a collapse during shock propagation (Phase II), as this phase is typically very short compared to Phase I and III, and a collapse is thus unlikely to occur.

approximately given by

$$\begin{aligned} \frac{dE_{\text{PWN}}}{dt} &= L_{\text{PWN}}(t) \\ &= \{1 - [1 - f_{\text{ej}}(t)]\mathcal{A}(t)\} f_{\text{beam}}(t) \frac{E_{\text{nth}}(t)}{t_{\text{diff,n}}(t)}, \end{aligned} \quad (107)$$

where, in analogy to Equation (57) the prefactor takes into account the combined effects of relativistic beaming and a non-zero albedo of the surrounding ejecta material.⁵ The total energy budget of the nebula thus evolves according to

$$\frac{dE_{\text{nth}}}{dt} = -L_{\text{PWN}}(t) + L_{\text{rad,in}}(t), \quad (108)$$

where $L_{\text{rad,in}}$ is the thermal radiation from the surrounding ejecta shell (see Equation (101)), and we can write the non-thermal radiation leaving the system as

$$L_{\text{rad,nth}}(x, t) = f_{\text{ej}}(t) L_{\text{PWN}}(x, t_{\text{coll}}) \frac{L_{\text{PWN}}(t)}{L_{\text{PWN}}(t_{\text{coll}})}. \quad (109)$$

In conclusion, after a collapse to a black hole, we evolve the system of evolution equations in Phase III assuming conservation of magnetic energy ($dE_{\text{B}}/dt = 0$), employing Equation (107) in Equation (14), and extending the set of Equations (11)–(15) by Equation (108) to evolve the nebula properties instead of solving Equations (78) and (79).

5. NUMERICAL PROCEDURE

In this section, we discuss several aspects related to the numerical evolution of the model presented in the previous sections. After briefly outlining the overall numerical procedure to integrate the evolution Equations (1)–(15) in Sections 5.1–5.3, we identify and define important timescales to be monitored during the numerical evolution (Section 5.4), discuss how to monitor the validity of neglecting synchrotron self-absorption (Section 5.5), discuss how to overcome problems related to stiffness in Equations (1)–(15) (Section 5.6), and finally discuss how to numerically compute the light curves as seen by a distant observer including relativistic effects such as relativistic beaming, the time-of-flight effect, and the relativistic Doppler effect (Section 5.7).

5.1. Hydrodynamic Wind Evolution

Prior to evolving the main evolution Equations (1)–(15), the evolution of the background fluid (the baryonic wind emitted during Phase I; see Section 4.1.1) has to be computed numerically. First, at any given time t the function $\bar{r}(r, t)$ is constructed solving Equation (28) numerically for every radius r . Knowing $\bar{r}(r, t)$ immediately yields the velocity profile $v_{\text{w}}(r, t)$ via Equation (30) and the mass profile $m_{\text{w}}(r, t)$ via Equation (27). By finite differencing the mass function $m_{\text{w}}(r, t)$ the corresponding density profile $\rho_{\text{w,t}}(r)$ is obtained (cf. Equation (29)). We typically employ a spatial grid ranging between $r = R_{\text{min}} = 30$ km and $R_{\text{ej}}(t)$ (cf. Equation (20)), which is logarithmically spaced with a fixed number of points per decade. Automatic mesh refinement (where needed) is used to resolve the profiles, which become increasingly “sharp” as

⁵ Prior to collapse in Phase III, the quasi-stationarity assumption in the present implementation of the radiative processes of the PWN (Section 4.3.1) prevent us from introducing these effects (see also Section 6).

Table 2

Model Input Parameters. Most of these Parameters can be Extracted from (or at Least Estimated/Constrained using) Numerical Relativity Simulations of BNS Mergers (see Section 3.1 and Table 1 of Paper II for a more Detailed Discussion)

Parameter	Description
\dot{M}_{in}	initial mass-loss rate of the NS (cf. Section 4.1.1)
t_{dr}	timescale for removal of differential rotation from the NS (cf. Section 4.1.1)
σ_M	ratio of t_{dr} to the timescale for decrease of the mass-loss rate (cf. Section 4.1.1)
$v_{\text{ej, in}}$	initial expansion speed of the baryonic ejecta material (cf. Section 4.1.1)
\bar{B}	magnetic field strength in the outer layers of the NS (cf. Equation (32))
η_{B_p}	dipolar magnetic field strength of the pulsar in units of \bar{B} (cf. Equation (41))
$E_{\text{rot, NS, in}}$	initial rotational energy of the NS (cf. Equation (42))
P_c	initial central spin period of the NS (cf. Equation (32))
R_e	equatorial radius of the NS (cf. Equation (32))
$M_{\text{NS, in}}$	initial mass of the NS (cf. Equation (45))
I_{pul}	moment of inertia of the pulsar (cf. Equation (46))
$\epsilon_{\text{ej, NS, in}}$	initial specific internal energy of the material ejected from the NS surface (cf. Equation (33))
κ	opacity of the ejecta material (cf. Equations (36), (71), (72), and (99))
$\mathcal{A}(\nu, t)$	frequency and time-dependent albedo of the ejecta shell in Phase II and III (cf. Sections 4.2.2 and 4.4)
t_ν	neutrino-cooling timescale (cf. Equation (33))
η_{B_n}	fraction of the total pulsar wind power injected as magnetic energy per unit time into the PWN (cf. Equations (10), (15), and Sections 4.2.2, 4.3.1).
η_{TS}	efficiency of converting pulsar wind power into random kinetic energy of accelerated particles in the PWN (cf. Equations (9), (76) and Sections 4.2.2, 4.3.1)
γ_{max}	maximum Lorentz factor for non-thermal particle injection into the PWN (cf. Section 4.3.1, Equation (76))
Γ_e	power-law index of the non-thermal spectrum for particle injection into the PWN (cf. Section 4.3.1, Equation (76))
f_{coll}	(only in the collapse scenario, Section 4.4) parameter specifying the time of collapse of the NS in units of the spin-down timescale (collapse during Phase III) or in units of t_{dr} (“ $f_{\text{coll, PT}}$ ”, collapse during Phase I)

the material moves outward to larger length scales. By employing this wind model the hydrodynamic evolution of the wind material has essentially been reduced to a numerical root finding problem.

The free parameters of the model, \dot{M}_{in} , t_{dr} , σ_M , and $v_{\text{ej, in}}$ are listed in Table 2. We note that numerical relativity simulations can be employed to directly determine \dot{M}_{in} and $v_{\text{ej, in}}$. Furthermore, they can provide estimates on t_{dr} . The only unconstrained parameter is σ_M , which controls the shape of the wind density profiles at later times. However, as the shock sweeps up all the material into a thin shell in Phase II, the exact distribution of matter is not important and does not influence the lightcurves and spectra of our model significantly.

5.2. PWN Balance Equations

At any time t in Phase III, the balance Equations (78) and (79) for the photon and non-thermal particle distribution in the PWN have to be solved. These distributions then specify, e.g., the source term dE_{PWN}/dt (cf. Equation (92)) required in Equation (14). We solve the coupled set of highly non-linear, integro-differential Equations (78)–(79) in analogy to the multi-step, iterative method outlined in Appendix B of LZ87. Only Step 1 of their method differs slightly from our Step 1 due to the modifications we introduced to the physical description of the pair plasma (cf. Section 4.3.1). Therefore, we rediscuss this step here for completeness and refer the reader to LZ87 for the other Steps.

Step 1 in solving Equations (78)–(79) consists of neglecting thermal Comptonization (i.e., setting $\dot{n}_C^T = 0$ in Equation (78)) and proceeds as follows.

- (i) Given an approximate photon spectrum $n(x)$ compute the corresponding particle distribution $N(\gamma)$ using Equation (83), where the integral over $P(\gamma)$ is computed using Equation (13) of LZ87.

- (ii) Compute

$$A(x) \equiv \frac{R_n}{c} (\dot{n}_0 + \dot{n}_A + \dot{n}_C^{\text{NT}} + \dot{n}_{\text{syn}})$$

using $N(\gamma)$ from (i), Equation (80), Equations (7), (8) (11), (15)–(18) of Svensson (1983), Equation (9) of LZ87, and Equation (87),

$$B(x) \equiv \frac{1}{1 + \frac{1}{3} \mathcal{T}_{\text{KN}}(x) f(x)} + \Delta \tau_C^{\text{NT}}$$

using Equations (21) and (10) of LZ87 together with $N(\gamma)$ from (i). Furthermore, compute

$$C(x) \equiv 0.2 R_n \sigma_T \frac{1}{x}$$

as well as $D(x) \equiv A(1/x)$, $E(x) \equiv B(1/x)$, and $F(x) \equiv C(1/x)$. We note that, with these definitions, all coefficient functions A, B, C, D, E, F are non-negative.

- (iii) Writing Equation (78) as $n(x) = A(x)/[B(x) + C(x)n(1/x)]$ and $n(1/x) = D(x)/[E(x) + F(x)n(x)]$ leads to a quadratic equation for $n(x)$,

$$BFn^2(x) + (BE + CD - AF)n(x) - AE = 0,$$

which has only one physical root,

$$n(x) = - \frac{(BE + CD - AF)}{2BF} + \frac{\sqrt{(BE + CD - AF)^2 + 4BFAE}}{2BF}. \quad (110)$$

Equation (110) is now used to update $n(x)$.

Initializing $n(x)$ by $(R_n/c)[\dot{n}_{0,\text{ej}} + f_{\text{ej}}\dot{n}_{0,\text{CMB}}]$, we iterate on Steps (i)–(iii) until for successive iterations $j - 1$ and j we have

$$\epsilon \equiv \|n(x)_j - n(x)_{j-1}\|_{\text{max}} < \epsilon_{\text{tol}}. \quad (111)$$

Here $\|u(x)\|_{\text{max}} = \max_{x \in X} |u(x)|$ for a function $u(x)$ on the dimensionless photon energy domain $X = [x_{\text{min}}, x_{\text{max}}]$ and typically $\epsilon_{\text{tol}} \leq 0.01$. As γ_{max} (cf. Equation (76)) is the maximum attainable photon energy, we set $x_{\text{max}} = \gamma_{\text{max}}$. In order to cover the frequency range down to the radio band, we typically set $x_{\text{min}} = 10^{-18}$. Both the particle energy and the photon energy domains are logarithmically spaced with typically 15 points per decade.

5.3. Evolving the Main Model

After having computed the hydrodynamic evolution of the baryonic wind (Section 5.1), its density profile $\rho_{w,t}(r)$ at any point in time and space is known and the main equations of our model (1)–(15) can be integrated. The time grid $T = [t_{\text{min}}, t_{\text{max}}]$ for this evolution is logarithmically spaced with typically 50 points per decade. Additional mesh refinement is used in order to properly resolve the propagation of the relativistic shock front through the ejecta material in Phase II. In our model, we associate the time of merger of the BNS system with $t = 0$, but start the numerical evolution from an appropriate final checkpoint of a numerical relativity simulation, corresponding to tens of milliseconds after merger, and evolve it over the timescales of interest until, e.g., $t_{\text{max}} \sim 10^7$ s. It is important to point out that numerical relativity simulations of BNS mergers can be employed to determine most of the input parameters of our model, which are listed in Table 2 (see Section 3.1 and Table 1 of Paper II for a more detailed discussion). Given those initial parameters read off or estimated from a simulation, the following evolution according to our model is a self-consistent prediction based on these initial conditions.

5.3.1. Phase I

In order to evolve Equations (1) and (2) from time t to $t + \Delta t$ we need to compute the source terms on the right-hand sides. This can be done in the following way:

- (i) Compute $v_w(R_{\text{ej}}(t), t)$ using the precomputed baryonic wind model (Section 5.1) or Equation (20).
- (ii) Employ the previously generated wind profiles $m_w(r, t)$ and $\rho_w(t)$ to compute the optical depth of the ejecta material (Equation (36)) and to numerically solve for the temperature of the ejecta material using Equation (39). This yields the source term $L_{\text{rad}}(t)$ (cf. Equations (34) and (35)).
- (iii) Compute the remaining two source terms using Equations (32) and (33).

This phase ends when $t = t_{\text{pul,in}}$ (Equation (40)) and Phase II starts. If the NS collapses to a black hole during Phase I, we keep evolving Equations (1) and (2), setting L_{EM} and $dE_{\text{th,NS}}/dt$ to zero (cf. Section 4.4).

5.3.2. Phase II

At $t = t_{\text{pul,in}}$, the initial rotational energy of the pulsar is computed using Equation (42) and its initial spin period is then inferred from Equation (46). This allows us to compute the initial spin-down luminosity (Equation (47)) and the spin-down

timescale (Equation (49)), which together define the spin-down luminosity at later times (Equation (48)).

In order to evolve the evolution Equations (3)–(10) from time t to $t + \Delta t$, one can proceed as follows:

- (i) Compute $v_w(R_{\text{ej}}(t), t)$ using the precomputed baryonic wind model (Section 5.1) or Equation (20).
- (ii) Compute $dE_{\text{th,vol}}$ and $v_{\text{sh}}(t)$ from Equations (62) and (58), respectively. Use $v_{\text{sh}}(t)$ and the wind profiles to evaluate shock heating according to Equation (63).
- (iii) Compute the source terms $L_{\text{sd}}(t)$, $L_{\text{rad,pul}}$, and dE_{PWN}/dt using Equations (48), (51), and (57).
- (iv) Find the temperatures of the shocked and unshocked ejecta parts by using the precomputed wind profiles $m_w(r, t)$, $\rho_w(t)$ and solving Equation (69). This yields the optical depths (Equations (71), (72)) and luminosities (73) and (74).
- (v) Evolve all quantities to $t + \Delta t$, except for R_n and E_{nth} .
- (vi) Define

$$E_{\text{nth}}(t + \Delta t) = E_{\text{nth}}(t) + \frac{dE_{\text{nth}}}{dt} \Delta t \quad (112)$$

$$R_n(t + \Delta t) = R_{\text{sh}}(t + \Delta t) \frac{E_{\text{th,sh}}(t + \Delta t)}{E_{\text{nth}}(t + \Delta t)} \quad (113)$$

and iterate until both quantities have converged to some desired accuracy. The second condition ensures pressure equilibrium between the nebula and the shocked ejecta layer (cf. Equation (61)).

Phase II ends when $R_{\text{sh}}(t + \Delta t) > R_{\text{ej}}(t + \Delta t)$.

5.3.3. Phase III

Once the shock has reached the outer ejecta layers, Phase III begins. The initial speed of the shocked ejecta layer is calculated from Equation (93). Evolving Equations (11)–(15) from time t to $t + \Delta t$ can be accomplished by the following steps:

- (i) Compute L_{sd} and $L_{\text{rad,pul}}$ using Equations (48) and (51).
- (ii) Compute the acceleration of the ejecta shell according to Equation (95).
- (iii) Find the temperature of the ejecta shell by solving Equation (96). This yields the optical depth (Equations (99)) and the luminosities L_{rad} and $L_{\text{rad,in}}$ (Equations (100) and (101)).
- (iv) Solve Equations (78) and (79) as described in Section 5.2 to find the source term dE_{PWN}/dt .

In the case the NS collapses to a black hole (see Section 4.4), Step (i) is omitted and Equation (108) is added as another evolution equation to Equations (11)–(15). Furthermore, Step (iv) is replaced by

- (iv)' Find the source term dE_{PWN}/dt using Equation (107).

This concludes our discussion of the overall procedure to evolve Equations (1)–(15).

5.4. Timescales

As our evolution model in Phase III is built upon the assumption of quasi-stationarity as far as radiative processes in the PWN are concerned, we need to monitor several timescales during the numerical evolution in order to assess the validity of this assumption. For these diagnostic purposes, we define the

following timescales in Phase III:

$$\tau_e(t) = \frac{l_e}{l_e}, \quad (114)$$

$$\tau_{\text{ph}}(t) = \frac{l_{\text{ph}}}{l_{\text{ph}}}, \quad (115)$$

$$\tau_c(\gamma, t) = \left| \frac{\gamma}{\dot{\gamma}_{\text{C,syn}}} \right|, \quad (116)$$

$$\tau_1(t) = \frac{R_n}{c}, \quad (117)$$

where γ denotes the Lorentz factor of a particle in the PWN and l_e , l_{ph} , and $\dot{\gamma}_{\text{C,syn}}$ are defined by Equations (76), (77), and (84), respectively.

In order for the stationarity assumption regarding the particle distribution to hold, which allowed us to integrate Equation (82) to obtain Equation (83), the timescale for equilibration of the particle distribution given by the cooling timescale τ_c has to be much smaller than any other timescale involved in the problem. In particular, it has to be smaller than the timescale for change of the photon distribution. Thus we have the requirements that

$$\tau_c(\gamma, t) \ll \tau_{\text{ph}}(t) \quad \forall t, \gamma, \quad (118)$$

$$\tau_c(\gamma, t) \ll \tau_e(t) \quad \forall t, \gamma. \quad (119)$$

Here, we have assumed that the timescales for change of the photon and particle distributions inside the nebula are approximately given by the timescales τ_{ph} and τ_e for change of the injected spectra. As we shall discuss in the companion paper (Paper II), we typically find that these conditions are very well satisfied across the entire parameter space in absence of significant acceleration of the ejecta shell after $t = t_{\text{shock,out}}$ and except for very late times $t \gtrsim 10^7$ s when the nebula has grown in size, the magnetic field strength has decreased, and synchrotron cooling has become less efficient. However, we are not interested in the evolution at these late times.

For the stationarity assumption regarding the photon spectrum to hold (i.e., for Equation (78) to hold), the timescale for the photon spectrum to change has to be much larger than the timescale for equilibration inside the nebula. As the positronic plasma inside the PWN is relativistic, its sound speed is close to the speed of light. We can thus assume that the nebula plasma adjusts to changing exterior conditions essentially on the timescale τ_1 . Therefore, one also has the requirement that

$$\tau_1(t) \ll \tau_{\text{ph}}(t) \quad \forall t. \quad (120)$$

As long as further acceleration of the ejecta shell after $t = t_{\text{shock,out}}$ is not significant, we typically find that this condition is well satisfied during the numerical evolution as we shall discuss in more detail in the companion paper (Paper II).

5.5. Synchrotron Self-absorption

In our model of the PWN in Phase III, we have neglected synchrotron self-absorption. In order to check the validity of this assumption during the numerical evolution of our model, we monitor the dimensionless photon energy $x_{\Delta\tau_{\text{syn}}=1}(t)$ defined by

$$\Delta\tau_{\text{syn}}(x_{\Delta\tau_{\text{syn}}=1}(t), t) = 1, \quad (121)$$

where $\Delta\tau_{\text{syn}}(x, t)$ is the approximate optical depth of the nebula to synchrotron self-absorption at time t (cf. Equation (88)). This dimensionless energy separates the optically thick and thin regimes of the photon spectrum and lies well below X-ray frequencies (typically by many orders of magnitude) as we shall discuss in the companion paper (Paper II). Therefore, the part of the spectrum that we are mostly interested in, i.e., at X-ray and γ -ray energies, is unaffected by effects of synchrotron self-absorption.

5.6. Stiffness Problem

At some point in the evolution (in Phase III), the photon diffusion timescale of the ejecta shell

$$t_{\text{diff,ej}} = \frac{R_{\text{ej}} - R_n}{c} (\Delta\tau_{\text{ej}} + 1) \quad (122)$$

becomes comparable to the temporal resolution Δt and Equation (14) becomes stiff. Here, $\Delta\tau_{\text{ej}}$ denotes the optical depth as seen from the lab frame (cf. Equation (103)). This problem can be noticed in the following way. Assuming $\Delta\tau_{\text{ej,com}} \gg 1$, a radiation dominated gas, such that $T_{\text{com}} \simeq E_{\text{th}}/aV_{\text{ej}}$ (cf. Equation (96)), and using Equations (98) and (100) it is straightforward to show that the thermal emission from the ejecta shell scales as $L_{\text{rad}} \propto E_{\text{th}}/t_{\text{diff,ej}}$. The photon diffusion timescale itself scales as $t_{\text{diff,ej}} \propto R_{\text{ej}}^{-2}$ (cf. Equation (99)). Hence, as R_{ej} is monotonically increasing with time, at some point $t_{\text{diff,ej}} \approx \Delta t$ and Equation (14) becomes stiff.

Fortunately, there is an easy way to bypass this problem. As $L_{\text{rad}} \propto E_{\text{th}}/t_{\text{diff,ej}}$, this term will eventually deplete the energy reservoir E_{th} of the ejecta shell until the shell enters an asymptotic regime in which the amount of injected energy equals the amount of emitted energy on the photon diffusion timescale. In other words, this regime is defined by setting $dE_{\text{th}}/dt = 0$ in Equation (14) on a timescale $t \sim t_{\text{diff,ej}}$. At any time in this asymptotic regime, the total internal energy E_{th} of the ejecta shell is then given by

$$E_{\text{th}}(t) = [1 - f_{\text{ej}}(t)] \frac{dE_{\text{PWN}}}{dt} t_{\text{diff,ej}}(t) \quad (123)$$

and a separate evolution equation for E_{th} is not needed anymore.

In practice, the grid spacing Δt has to be adjusted such that this asymptotic regime is reached well before $\Delta t \approx t_{\text{diff,ej}}$. Once this is achieved, we typically switch to the asymptotic regime during the numerical evolution at t_{res} , defined by $t_{\text{diff,ej}}(t_{\text{res}}) = 2\Delta t$. By definition of this regime, L_{rad} and $L_{\text{rad,in}}$ scale as dE_{PWN}/dt . Therefore, assuming that the thermal photons from the ejecta shell dominate the photon injection l_{ph} of the PWN (cf. Equation (77)), l_{ph} is expected to scale as l_e . As the PWN conserves energy (total luminosity of injection equals the luminosity of emitted radiation; see Appendix A.4) we hence conclude that

$$\frac{dE_{\text{PWN}}}{dt} \propto (L_{\text{sd}} + L_{\text{rad,pul}}). \quad (124)$$

In order to avoid numerical runaway instabilities due to the fact that dE_{PWN}/dt in Equation (123) depends on the solution to Equations (78) and (79), which, in turn, depends on the injected

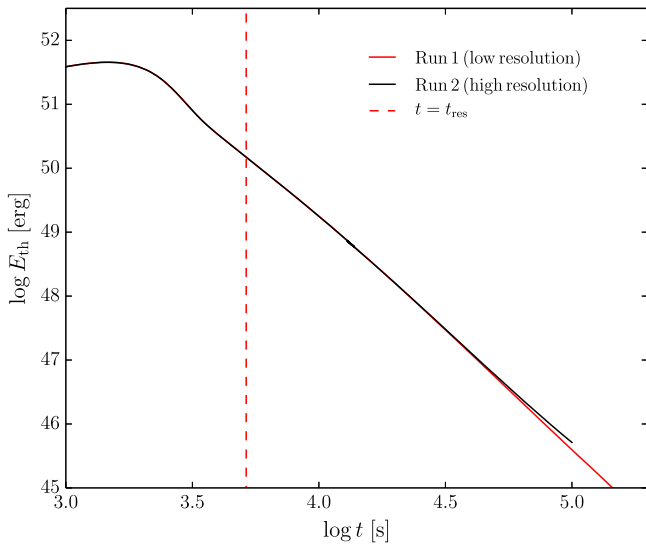


Figure 3. Evolution of the internal energy E_{th} of the ejecta shell in Phase III according to a run using the evolution scheme described in this section (Run 1) and a run using additional mesh refinement to evolve Equation (14) up to late times (Run 2). The dashed red line indicates the time of transition $t = t_{\text{res}}$ to the modified evolution scheme for Run 1.

photons, i.e., on dE_{PWN}/dt , we employ Equation (124) in Equation (123) and calibrate the prefactor at t_{res} to ensure continuity over $t = t_{\text{res}}$. This calibration, however, is only valid for $t > t_{\text{res}}$ if also the dynamics of the shell have reached an asymptotic regime, i.e., if no further acceleration occurs such that, e.g., the beaming factor does not depend on time. In practice, a grid spacing can always be set up to satisfy this constraint as well.

Figure 3 compares the internal energy E_{th} of a typical model case evolved using the scheme outlined above (Run 1) with the corresponding result for a simulation in which a power-law refinement $\Delta t \propto t_{\text{diff,ej}} \propto R_{\text{ej}}^{-2}$ was implemented (Run 2). For the latter run, the refinement guaranteed $\Delta t \ll t_{\text{diff,ej}}$ at all times and thus allowed us to integrate Equation (14) for all times. The agreement between the two runs is remarkably good and indicates that the scheme described above well captures the evolution of the system at later times than t_{res} . Remaining discrepancies at late times $t \sim 10^5$ s are due to numerical errors as the ever decreasing time step in Run 2 results in increasing accuracy for the time integrations of Equations (11)–(15). Finally, we note that runs with power-law refinement are computationally very expensive, such that comparisons like the one presented here cannot be carried out routinely and we will thus not add this comparison to the set of routine checks (see Sections 5.4 and 5.5) that we shall discuss in more detail in the companion paper (Paper II).

5.7. Observer Lightcurve Reconstruction

This section is devoted to a discussion of how the lightcurve and spectra as seen by a distant observer can be reconstructed, including relativistic effects such as the relativistic Doppler effect, the time-of-flight effect, and relativistic beaming. As the effective temperature of blackbody radiation is altered by the relativistic Doppler factor and enters the luminosity to the fourth power, even mildly relativistic ejecta shell velocities of $v_{\text{ej}} \sim 0.1c$ can have a significant influence on the lightcurve. Furthermore, as the PWN and the ejecta shell expand to large

radii, radiation reaching the observer from different locations on the surface of the expanding sphere can have appreciable delays. These delays are particularly important in dynamical situations, in which the ejecta shell is accelerated or in which the NS collapses to a black hole and induces an abrupt change in the radiation escaping from the system. Finally, relativistic beaming is influential in the sense that it normalizes the total luminosity by selecting an effective surface area of the expanding sphere that emits in the direction of the observer. In so doing, it also affects the maximum delay concerning the time-of-flight effect and must therefore be taken into account. Consequently, it is important to consider these relativistic effects when predicting observer lightcurves and spectra with our model.

We numerically compute the lightcurves and spectra as seen by a distant observer including the relativistic effects described above by decomposing the radiation originating from the surface area of the half-sphere facing the observer into individual energy packages released at time t during a time Δt from ring-shaped portions of surface area of equal distance to the observer. These packages are emitted at time t and then recollected by the observer according to their time of flight and their Doppler-shifted frequency. To this end, we define a coordinate system centered about the NS, with its z -axis in direction of the remote observer and θ denoting the polar angle. At any time t let us consider two half spheres facing the observer, defined by $\theta \in [0, \pi/2]$ and radii $R_{\text{ej}}(t)$ and $R_{\text{n}}(t)$, respectively. Due to relativistic beaming, only radiation originating from the regions $\theta \in [0, \theta_{\text{max}}(t)]$ will eventually reach the observer (Rees 1966), where

$$\theta_{\text{max}}(t) = \arccos\left(\frac{v_{\text{ej}}(t)}{c}\right). \quad (125)$$

This area is then further decomposed into rings of constant θ , defined by a grid $\Theta = [0, \dots, \theta_k, \dots, \theta_{\text{max}}(t)]$, with n_{θ} points and spacing $\Delta\theta_k$ that is equidistant in the limb angle $\mu = \cos\theta$.

Moreover, given a time grid $T = [t_{\text{min}}, \dots, t_i, \dots, t_{\text{max}}]$ for the evolution of Equations (1)–(15) appropriate to properly resolve the shock dynamics during Phase II and to overcome the stiffness problem (cf. Section 5.6), we define a time grid for the observer $T' = [t'_{\text{min}} = t_{\text{min}}, \dots, t'_j, \dots, t'_{\text{max}} = t_{\text{max}}]$ by

$$t'_0 = t'_{\text{min}}, \quad (126)$$

$$t'_{j+1} = t'_j + N'_j \frac{v_{\text{ej,in}} t'_j}{cn_{\theta}}, \quad (127)$$

where $N'_j < 1$. In order for the observer to resolve the time-of-flight effect, i.e., to distinguish between the various energy contributions from different locations on the emitting surface area, the grid spacing $\Delta t'$ at time t' has to be smaller than the light crossing time of the half sphere divided by the number of individual rings. Since

$$\Delta t'_j = N'_j \frac{v_{\text{ej,in}} t'_j}{cn_{\theta}} < \frac{R_{\text{ej}}(t'_j)}{cn_{\theta}}, \quad (128)$$

the grid spacing defined by Equation (127) guarantees that the time-of-flight effect is properly resolved.

We also define a receiver energy grid $E'(T', X')$ for the remote observer, where X' denotes the grid in dimensionless energy $x' = hv'/m_e c^2$, which is typically similarly spaced as the corresponding one used in the evolution of the main model

(cf. Section 5.2). The energy contribution of a ring of width $d\theta$ at θ to the total energy emission during a time dt per unit frequency as measured by the distant observer is given by

$$\frac{dE'}{d\nu'} = 4\pi I'(\nu') d\sigma \cos \theta_{\text{com}} dt, \quad (129)$$

where $I'(\nu')$ is the specific intensity as seen by the observer, $d\sigma = 2\pi R_{\text{ej}/n}^2 \sin \theta d\theta$ is the surface area of the ring, and θ_{com} given by

$$\tan \theta_{\text{com}} = \sqrt{1 - v_{\text{ej}}^2/c^2} \frac{\sin \theta}{\cos \theta - v_{\text{ej}}/c} \quad (130)$$

defines the direction of the observer as seen in the local comoving frame of the expanding surface. We note that the effective emitting surface area $d\sigma \cos \theta_{\text{com}}$ approaches zero as θ reaches θ_{max} . We have already multiplied by 4π in Equation (129) to account for an isotropic source.

According to the relativistic Doppler effect applied to a photon of frequency ν emitted from the surface at a point specified by an angle θ in direction of the remote observer,

$$D \equiv \frac{\nu'}{\nu} = \frac{x'}{x} = \frac{\sqrt{1 - v_{\text{ej}}^2/c^2}}{1 - (v_{\text{ej}}/c) \cos \theta}. \quad (131)$$

Noting that I/ν^3 is Lorentz invariant, where I is the specific intensity, we have $I' = D^3 I$. Therefore, for the blackbody emission of the ejecta material,

$$I'_{\text{th}}(\nu') = \frac{2 h \nu'^3}{c^2} \left[\exp\left(\frac{h\nu'}{D k_{\text{B}} T_{\text{eff,com}}}\right) - 1 \right]^{-1}, \quad (132)$$

where $T_{\text{eff,com}}$ is given by Equation (98). We note that the effective temperature as seen by the distant observer is thus $T'_{\text{eff}} = D T_{\text{eff,com}}$. Since the associated luminosity scales as $L' \propto D^4 T_{\text{eff,com}}^4$, small deviations of D from unity can already have an appreciable influence on the observer lightcurve. Furthermore, as long as the nebula is optically thick, i.e., $\Delta\tau_{\text{T}} > 1$, the escaping photons originate from the outer surface layer at $r = R_{\text{n}}$ and we can set

$$I'_{\text{nth}}(x') = D^3 \frac{L_{\text{rad,nth}}(x'/D, t)}{4\pi R_{\text{n}}^2} \quad (133)$$

for the non-thermal radiation, with $L_{\text{rad,nth}}(x, t)$ being the non-thermal luminosity of the nebula (cf. Equations (104) and (109)). When beaming is already encoded in $L_{\text{rad,nth}}(x, t)$ itself (cf. Section 4.4), the right-hand side of Equation (133) has to be divided by f_{beam} to solely take the geometric time-of-flight effect into account (through the subdivision into individual rings up to $\theta = \theta_{\text{max}}$).

When the nebula is optically thin, i.e., $\Delta\tau_{\text{T}} < 1$, the escaping photons are emitted uniformly and isotropically throughout the volume of the nebula. In this case, we slice the nebula volume V_{n} into spherical shells of radius $r \in R = [R_{\text{min}}, R_{\text{n}}]$ and thickness dr and subdivide each shell into rings of constant $\theta_{\text{vol}} \in \Theta_{\text{vol}} = [0, \pi]$ and width $d\theta_{\text{vol}}$. The contribution of such volume elements $dV = d\sigma dr = 2\pi r^2 \sin \theta_{\text{vol}} d\theta_{\text{vol}} dr$ to the total energy emission during a time dt per unit frequency as

measured by the distant observer can then be written as

$$\frac{dE'}{dx'} = D^3 L_{\text{rad,nth}}(x'/D, t) \frac{dV}{V_{\text{n}}} dt. \quad (134)$$

Here, D is defined as in Equation (131) in terms of the local velocity $v(r) = v_{\text{ej}} r/R_{\text{n}}$.

With these definitions and expressions at hand, we compute the radiation emitted at time t during a time Δt as received by the remote observer according to the following steps:

- (i) First, compute the arrival times of the energy packages for all emitting rings and spherical segments, i.e., for all $\theta \in \Theta$, $\theta_{\text{vol}} \in \Theta_{\text{vol}}$, and $r \in R$:

$$t'_{\text{arr,th}}(\theta) = \frac{R_{\text{min}}}{c} + t - \frac{R_{\text{ej}}(t)}{c} \cos \theta \quad (135)$$

$$t'_{\text{arr,nth,surf}}(\theta) = \frac{R_{\text{min}}}{c} + t - \frac{R_{\text{n}}(t)}{c} \cos \theta \quad (136)$$

$$t'_{\text{arr,nth,vol}}(\theta_{\text{vol}}, r) = \frac{R_{\text{min}}}{c} + t - \frac{r}{c} \cos \theta_{\text{vol}}. \quad (137)$$

This definition of arrival times ensures that a photon emitted at $t = t_{\text{min}}$ from the outer surface of the baryonic wind at $R_{\text{ej}}(t_{\text{min}}) = R_{\text{min}}$ and $\theta = 0$ reaches the observer at $t' = t_{\text{min}}$.

- (ii) Second, compute the energy spectrum $\Delta E'_{\text{th}}(\Theta, X')$ that is generated by thermal radiation from the surface of the ejecta matter using Equations (129) and (132):

$$\Delta E'_{\text{th}}(\theta_k, \nu'_l) = 8\pi^2 R_{\text{ej}}^2 I'_{\text{th}}(\nu'_l) \times \sin \theta_k \cos[\theta_{\text{com}}(\theta_k)] \Delta\theta_k \Delta t. \quad (138)$$

- (iii) In analogy to the thermal radiation in Step (ii), use Equations (129), (133), and (134) to compute the energy contributions generated by the non-thermal radiation from the PWN once the ejecta shell has become optically thin:

$$\begin{aligned} \Delta E'_{\text{nth,surf}}(\theta_k, x'_l) &= (1 - f_{\text{n}}) 8\pi^2 R_{\text{n}}^2 I'_{\text{nth}}(x'_l) \\ &\quad \times \sin \theta_k \cos[\theta_{\text{com}}(\theta_k)] \Delta\theta_k \Delta t \\ \Delta E'_{\text{nth,vol}}(\theta_{\text{vol,k}}, x'_l, r_m) &= f_{\text{n}} \frac{3}{2} D^3 L_{\text{rad,nth}}(x'_l/D) \\ &\quad \times \frac{r_m^2}{R_{\text{n}}^3} \sin \theta_{\text{vol,k}} \Delta\theta_{\text{vol,k}} \Delta r_m \Delta t. \end{aligned} \quad (139)$$

The function $f_{\text{n}}(t)$ is defined in terms of $\Delta\tau_{\text{T}}$ in analogy to f_{ej} in Equation (102). It is used here to guarantee a smooth transition between the optically thick and thin regimes of the nebula, corresponding to surface and volume nebula emission, respectively.

- (iv) Use the mapping of angles to arrival times from Step (i) to put the energy packages from Steps (ii) and (iii) into the correct time and frequency bins of the observer energy grid $E'(T', X')$.

Once the evolution of Equations (1)–(15) has been accomplished up to $t = t_{\text{max}}$ and all energy packages have been sent and received, the energy array of the observer, $E'(T', X')$, may be divided by the time steps $\Delta t'_j$ to obtain the corresponding observer luminosity

$$L_{\text{obs}}(t'_j, x'_l) = E'(t'_j, x'_l) / \Delta t'_j. \quad (140)$$

This quantity can then be used to compute detailed predictions for the luminosity as seen by a remote observer in specific wavelength bands, such as in the γ -ray, X-ray, UV, optical, and radio bands (see [Paper II](#)).

6. DISCUSSION AND CONCLUSION

In this paper, we have presented a dynamical model to describe the post-merger evolution of a BNS system and its EM emission. Our model assumes that the merger of two NSs leads to the formation of a (hypermassive, supramassive, or stable) NS which does not collapse to a black hole on timescales of at least tens of milliseconds after merger. As we have argued (cf. Section 1), such a long-lived NS is a very likely possibility, such that the model should be applicable to a large fraction of BNS merger events. In contrast to a black hole promptly formed after merger and surrounded by a short-lived accretion disk, such long-lived objects can power long-lasting EM emission from γ -ray to radio energies that might be responsible for at least part of the observed long-lasting afterglow emission observed in many SGRBs. We refer to [Paper II](#) for a detailed account on modeling X-ray afterglow lightcurves with our model in the context of SGRBs. Moreover, this model also represents an important tool to identify EM counterparts associated with the GW signal of the inspiral and merger of a BNS system (see [Paper II](#) for a detailed discussion). The identification of such EM counterparts is essential for performing joint EM and GW observations. Joint observations involving EM counterparts of the kind discussed here (long-lasting and highly isotropic) can confirm the association of the GW signal with a BNS merger (i.e., distinguish from the NS–BH binary merger). With the advanced LIGO/Virgo detector network starting its first science run later this year, such multimessenger astronomy will turn into exciting reality in the very near future.

Our model is formulated in terms of a set of highly coupled differential equations, which provide a self-consistent evolution of the post-merger system and its EM emission given some initial data. Such initial data can be extracted from a numerical relativity simulation of the merger and early post-merger phase at a few to tens of milliseconds after the merger, once a roughly axisymmetric state has been reached. Our model allows us to evolve the post-merger system over time and lengthscales inaccessible to numerical relativity simulations, typically up to $\sim 10^7$ s after merger. It thus bridges the gap between numerical relativity simulations of the merger process and the timescales of interest for SGRB afterglow radiation. The model evolves the system through three main evolutionary phases: an early baryonic wind phase (Phase I), a pulsar wind shock phase (Phase II), and a PWN phase (Phase III). Furthermore, the possibility of collapse to a black hole during any of the three phases is accounted for. Our model links the evolution of the central engine directly to the observed afterglow radiation, taking into account relativistic dynamics as well as an accurate reconstruction of the observer lightcurve including relativistic beaming, the relativistic Doppler and the time-of-flight effect.

Prompt SGRB emission and time-reversal scenario—Our model makes no assumption on how and when the prompt γ -ray emission of the SGRB itself is produced. It can accommodate both the standard scenario (SGRB at the time of merger) and the recently proposed time-reversal scenario (SGRB at the time of collapse of the remnant NS; [Ciolfi & Siegel 2015a, 2015b](#)). It can obviously also accommodate the

case in which no relativistic jet and thus no SGRB is produced at all.

In the context of magnetar models for SGRBs, the prompt emission is assumed to be generated by an accretion powered relativistic jet emerging from a NS–torus system shortly (\sim ms) after the time of merger (e.g., [Metzger et al. 2008](#); [Bucciantini et al. 2012](#); [Gompertz et al. 2014](#); [Metzger & Piro 2014](#); [Gao et al. 2015](#)). However, a generic feature of a newly-born NS after a BNS merger will be strong baryon pollution in its vicinity due to dynamical ejecta from the merger process and neutrino and magnetically driven winds from its surface or possibly from an accretion disk ([Oechslin et al. 2007](#); [Dessart et al. 2009](#); [Bauswein et al. 2013](#); [Hotokezaka et al. 2013](#); [Metzger & Fernández 2014](#); [Siegel et al. 2014](#); [Kastaun & Galeazzi 2015](#); see Section 4.1). Such baryon pollution can not only choke jets ([Murguia-Berthier et al. 2014](#); [Nagakura et al. 2014](#)), but it is likely to even prevent the generation of any relativistic outflow at all. We note that numerical simulations of BNS mergers that lead to the formation of a remnant NS have not found indications for the generation of a relativistic jet ([Giacomazzo & Perna 2013](#)).

In the time-reversal scenario, the SGRB is generated at the time of collapse of the supramassive remnant NS. In this case, the baryon-free PWN surrounding the collapsing NS does not threaten the formation of an accretion powered jet from the remaining BH–torus system. [Margalit et al. \(2015\)](#) have recently argued that the formation of an accretion disk following the collapse of the supramassive NS is rather unlikely. However, numerical simulations will be needed to further investigate this issue.

As there are still many open questions related to the formation of the SGRB prompt emission in BNS mergers, our model is designed to be general in the sense that it does not make assumptions on the generation of the prompt emission. In either scenario, it provides detailed predictions for the intrinsic afterglow emission emerging from the post-merger system that can be compared to observations (see [Paper II](#)). In the time-reversal scenario, it additionally predicts the EM emission prior to the SGRB itself (see [Paper II](#)). If such emission is found, it would represent strong evidence in favor of the time-reversal scenario (see Section 7 of [Paper II](#) for a more detailed discussion and implications for joint GW and EM observations).

Comparison to earlier work—Other authors, e.g., [Yu et al. \(2013\)](#) and [Metzger & Piro \(2014\)](#), have previously considered radiation from a similar physical setup.⁶ During the time of writing also [Gao et al. \(2015\)](#) have investigated EM emission in a similar context. All of the aforementioned authors considered a setup that is qualitatively similar to the phenomenology in Phase III of our model: a remnant NS (previously born in a BNS merger), surrounded by a PWN that is confined by a shell of matter. They present different models to evolve such a setup and to predict thermal and non-thermal radiation emerging from such a system. Based on a simple dynamical model, [Yu et al. \(2013\)](#) find thermal emission peaking around $\sim 10^4$ – 10^5 s after merger with luminosities of $\sim 10^{44}$ – 10^{45} erg s^{−1}, which they term “merger-nova”. Building on this model, [Gao et al. \(2015\)](#) argue that such a merger-nova is consistent with the late-time rebrightening observed at optical and X-ray

⁶ [Gao et al. \(2013\)](#) have also considered a similar scenario, but focus on computing afterglow radiation from the interaction of ejected mass with the ambient medium.

wavelengths in GRB 080503. Metzger & Piro (2014) consider a more detailed physical model, in particular, regarding the PWN physics, but without relativistic dynamics. Furthermore, they implement a detailed formalism to compute the ejecta opacities, the degree of ionization, and the resulting albedo in a self-consistent way. As a result of a more detailed physical description of the PWN and its interaction with the ejecta layer, Metzger & Piro (2014) obtain a dimmer thermal optical/UV transient peaking at a luminosity of $\sim 10^{43}$ – 10^{44} erg s $^{-1}$ on a timescale of $\sim 10^4$ – 10^5 s after merger and argue that the late-time X-ray excess of GRB 130603B (Fong et al. 2014) as well as the late-time optical rebrightening and X-ray emission of GRB 080503 is consistent with their model.

In contrast to previous work, we start the evolution shortly after the BNS merger and introduce a first baryonic wind phase that we expect to be generic of BNS mergers leading to the formation of a long-lived remnant NS. Furthermore, we introduce the pulsar ignition and pulsar wind shock phase (qualitatively similar to the initial phase of Metzger et al. 2014). As the pulsar wind shock is propagating at relativistic speeds in our setup, we implement a relativistic scheme to describe the propagation across the ejecta and a detailed description of the energy transfer between the PWN, the shock heated, and unshocked ejecta during this phase. In Phase III, we implement a self-consistent model for the radiative processes occurring in the PWN, including pair creation and annihilation, Compton scattering, Thomson scattering, and synchrotron cooling. Moreover, we employ a relativistic description of the dynamics in terms of a Milne-universe model and develop a reconstruction of the observer lightcurve and spectra taking into account the combined effects of relativistic beaming, the relativistic Doppler effect, and the time-of-flight effect. As a result of baryon pollution being a general feature and the level of detail reached here, we expect our model to be applicable to a much larger class of SGRBs than previously thought. We explore this possibility in Paper II. In particular, we point out that previous magnetar models, which are applied to large classes of SGRB events (e.g., Gompertz et al. 2013, 2014; Rowlinson et al. 2013; Lü et al. 2015) neglect the effects of surrounding ejecta material on the magnetar emission and instead assume a direct and instantaneous conversion of spin-down energy L_{sd} into observed X-ray luminosity L_X by some unspecified process, $L_{\text{sd}} \propto L_X$. This typically leads to very simple analytical fitting formulae for the X-ray lightcurves, which is in sharp contrast to the self-consistent dynamical evolution considered here.

Rayleigh–Taylor instability, kick velocities, and PWN jet—Our model is one-dimensional and highly idealized. As noted by Metzger & Piro (2014), at early times the high pressure of the PWN pushing against the ejecta shell can trigger a Rayleigh–Taylor instability. This would presumably cause some porosity in the ejecta envelope thanks to which non-thermal radiation from the PWN could escape from the system already at much earlier times. Such effects, however, are difficult to take into account in a one-dimensional model like ours and are neglected here.

Another deviation from spherical symmetry not accounted for by our one-dimensional model could arise from the possible presence of a kick velocity of the newly-formed NS. A large kick velocity could qualitatively alter the evolutionary scenario considered here.

Furthermore, based on axisymmetric magnetohydrodynamic simulations, Bucciantini et al. (2012) show that for sufficiently high spin-down energies, the built-up of strong toroidal magnetic field in the PWN interior can drive a bipolar jet through the ejecta shell and might even disrupt it entirely. Such jet breakouts were employed by Bucciantini et al. (2012) to model SGRBs with extended emission. However, recent three-dimensional simulations indicate that such jet breakouts are an intrinsic effect of two-dimensional simulations, and that the kink instability in three-dimensions destroys the polar jets and dissolves them into the PWN (Porth et al. 2014). Therefore, we exclude such catastrophic events for our model.

Future improvements—Our model already reflects a certain degree of detail and sophistication, but many aspects can be improved in future work. A more accurate description of radiative transfer through the ejecta shell and the PWN is required to predict more accurate lightcurves and spectra, which would be desirable for a more detailed comparison with observational data. Furthermore, the present implementation of a self-consistent modeling of the radiative processes occurring in the PWN requires the assumption of quasi-stationarity (as far as those processes are concerned). In the future, it would be desirable to develop a time-dependent formalism, which would then allow us to include a self-consistent computation of a time and frequency-dependent albedo of the ejecta material (similar to Metzger & Piro 2014). Moreover, such a time-dependent formalism would more accurately describe further acceleration of the ejecta shell in Phase III, it would allow us to include the associated pdV work done by the nebula, and it would provide a more accurate model of the PWN emission during the transient phase following the collapse of the remnant NS. Finally, we note that with different initial data and some modifications, our model could also be employed to investigate EM afterglows of long GRBs.

We thank B.F. Schutz, W. Kastaun, B.D. Metzger, and N. Bucciantini for valuable discussions. R.C. acknowledges support from MIUR FIR Grant No. RBFR13QJYF.

APPENDIX

A.1. Relativistic Rankine–Hugoniot conditions

This appendix is devoted to deriving Equations (58), (59), (60), and (64) from the special-relativistic Rankine–Hugoniot conditions (e.g., Taub 1948; Marti et al. 1994), thereby also rederiving some of the expressions in Taub (1948) using our notation and conventions. The Rankine–Hugoniot conditions were obtained in the special-relativistic case by Taub (1948) and relate the fluid properties across a shock wave imposing continuity of the mass and energy-momentum flux:

$$[\rho u^\mu] n_\mu = 0, \quad (141)$$

$$[T^{\mu\nu}] n_\mu = 0. \quad (142)$$

Here, $[f] = f_R - f_L$ relates the values of a quantity f on one side and the other side of the discontinuity surface with normal vector n^μ . We choose a frame in which the shock is at rest and adopt Cartesian coordinates such that $n^\mu = (0, 1, 0, 0)$. Furthermore, we assume an ideal fluid with rest-mass density ρ , pressure p , specific internal energy ϵ , four-velocity $u^\mu = (\gamma, \gamma u, 0, 0)$, where $\gamma = (1 - u^2)^{-1/2}$, and energy-

momentum tensor $T^{\mu\nu} = \rho(c^2 + \epsilon + p/\rho)u^\mu u^\nu + p\eta^{\mu\nu}$, where $\eta^{\mu\nu} = \text{diag}(-1, 1, 1, 1)$ is the Minkowski metric. Finally, we assume an ideal gas equation of state, $p = (\Gamma - 1)\rho\epsilon$, where Γ denotes the adiabatic index. Under these assumptions, the Rankine–Hugoniot conditions (Equations (141) and (142)) are written as (cf. also Taub 1948)

$$\frac{\rho_L u_L}{\sqrt{1 - u_L^2}} = \frac{\rho_L u_R}{\sqrt{1 - u_L^2}} \equiv m, \quad (143)$$

$$\begin{aligned} \rho_L \left(c^2 + \frac{\Gamma}{\Gamma - 1} \frac{p_L}{\rho_L} \right) \frac{u_L}{1 - u_L^2} \\ = \rho_R \left(c^2 + \frac{\Gamma}{\Gamma - 1} \frac{p_R}{\rho_R} \right) \frac{u_R}{1 - u_R^2}, \end{aligned} \quad (144)$$

$$\begin{aligned} p_R - p_L = m^2 c^2 \left[\frac{1}{\rho_L} \left(1 + \frac{\Gamma}{\Gamma - 1} \frac{p_L}{\rho_L c^2} \right) \right. \\ \left. - \frac{1}{\rho_R} \left(1 + \frac{\Gamma}{\Gamma - 1} \frac{p_R}{\rho_R c^2} \right) \right]. \end{aligned} \quad (145)$$

We note that for a mixture of radiation and ideal gas with $\Gamma = 4/3$ (i.e., the ejecta matter considered in our model), the Rankine–Hugoniot conditions take exactly the same form, with p_L and p_R being replaced by the respective sums of the radiation and fluid pressures.

Squaring Equation (144) and subtracting Equation (145) multiplied by $m^2[\dots]$ yields (where $[\dots]$ denotes the square bracket on the right hand side of Equation (145) with a + sign separating the two terms; cf. also Equation (7.8) in Taub 1948):

$$\begin{aligned} c^2 \left[\left(1 + \frac{\Gamma}{\Gamma - 1} \frac{p_L}{\rho_L c^2} \right)^2 - \left(1 + \frac{\Gamma}{\Gamma - 1} \frac{p_R}{\rho_R c^2} \right)^2 \right] \\ = (p_L - p_R) \left[\frac{1}{\rho_L} \left(1 + \frac{\Gamma}{\Gamma - 1} \frac{p_L}{\rho_L c^2} \right) \right. \\ \left. - \frac{1}{\rho_R} \left(1 + \frac{\Gamma}{\Gamma - 1} \frac{p_R}{\rho_R c^2} \right) \right]. \end{aligned} \quad (146)$$

This equation can be read as a quadratic equation for ρ_L in terms of ρ_R , p_L , and p_R . In the following, we assume a strong shock, i.e.,

$$p_L \gg p_R, \quad (147)$$

and a non-relativistic fluid ahead of the shock, i.e.,

$$p_R/(\rho_R c^2) \ll 1. \quad (148)$$

These assumptions are very well satisfied for the pulsar wind shock in Phase II (see Section 4.2.3), given the non-relativistic unshocked ejecta ahead of the shock front and the very high nebula pressure p_n (Equation (53)) that equals the pressure p_L of the shocked ejecta according to the pressure balance condition (61). With these assumptions, we obtain

Equation (60) from Equation (146):

$$\rho_L = \frac{\Gamma + 1}{\Gamma - 1} \rho_R \frac{1}{2} \left\{ 1 + \left[1 + 4 \frac{p_L}{\rho_R c^2} \frac{\Gamma}{(\Gamma + 1)^2} \right]^{\frac{1}{2}} \right\}. \quad (149)$$

With the help of Equation (143), Equation (145) can be written as

$$\begin{aligned} \frac{u_R^2}{1 - u_R^2} &= \frac{\frac{p_L}{\rho_R c^2} \left(1 - \frac{p_R}{p_L} \right)}{1 - \frac{\rho_R}{\rho_L} + \frac{\Gamma}{\Gamma - 1} \left(\frac{p_R}{\rho_R c^2} - \frac{\rho_R}{\rho_L} \frac{p_L}{\rho_L c^2} \right)} \\ &= \frac{\rho_R^2}{\rho_L^2} \frac{u_L^2}{1 - u_L^2}, \end{aligned} \quad (150)$$

from which using Equations (147) and (148) we obtain:

$$|u_R| = \left\{ \frac{p_L}{\rho_R c^2} \left[1 - \frac{\rho_R}{\rho_L} \left(1 + \frac{\Gamma}{\Gamma - 1} \frac{p_L}{\rho_L c^2} \right) + \frac{p_L}{\rho_R c^2} \right]^{-1} \right\}^{\frac{1}{2}}, \quad (151)$$

$$|u_L| = \left\{ \frac{p_L}{\rho_L c^2} \left[\frac{\rho_L}{\rho_R} - 1 - \frac{1}{\Gamma - 1} \frac{p_L}{\rho_L c^2} \right]^{-1} \right\}^{\frac{1}{2}}. \quad (152)$$

In our setup, $u_R < 0$, i.e., the fluid ahead of the shock is moving toward the shock in the rest frame of the shock front. As seen from the frame comoving with the fluid ahead of the shock, the shock velocity $v_{\text{sh},R}$ is then given by $v_{\text{sh},R} = |u_R|c$ (Equation (59)). In order to obtain the shock speed in the lab frame, we apply a Lorentz transformation and arrive at Equation (58). Accordingly, we have $u_L > 0$ and the velocity of the fluid behind the shock as seen from the frame comoving with the shock front is given by $v_L = u_L c$ (this quantity is needed in Equation (68)).

For the jump in specific internal energy across the shock, we have

$$\frac{\Delta\epsilon}{c^2} = \frac{\epsilon_L - \epsilon_R}{c^2} = \frac{1}{\Gamma - 1} \left(\frac{p_L}{\rho_L c^2} - \frac{p_R}{\rho_R c^2} \right). \quad (153)$$

Using Equations (147), (148), and (149) this results in

$$\Delta\epsilon = \frac{1}{\Gamma + 1} \frac{p_L}{\rho_R} \frac{2}{1 + \left[1 + \frac{4\Gamma}{(\Gamma + 1)^2} \frac{p_L}{\rho_R c^2} \right]^{\frac{1}{2}}}, \quad (154)$$

which is the desired expression in Equation (64).

A.2. Transformation between Comoving and Lab Frame

This appendix defines the lab and comoving frames used in Phase III of our evolution model to describe the expansion of the ejecta shell (cf. Section 4.3.2) and it provides transformations for some quantities required by our model. The Milne universe metric has recently been employed to describe an expanding homogeneous GRB fireball (Li 2007, 2013). We follow this approach and apply it to the expansion of a thin ejecta shell. Some of the expressions that we derive here are

based on expressions discussed by Li (2007, 2013), some of which we shall rederive here for completeness.

Let $X^\mu = (ct, r, \theta, \phi)$ denote the rest frame of the NS (or the “lab frame”) with spherical coordinates and Minkowski metric $g_{\mu\nu} = \text{diag}(-1, 1, r^2, r^2 \sin^2 \theta)$. Now consider the following coordinate transformation $X^\mu \mapsto X'^\mu = (c\eta, \xi, \theta, \phi)$, defined by

$$t = \eta \cosh \xi, \quad r = c\eta \sinh \xi, \quad (155)$$

which transforms the Minkowski metric into $g'_{\mu\nu} = \text{diag}(-1, a^2(\eta), a^2(\eta) \sinh^2 \xi, a^2(\eta) \sinh^2 \xi \sin^2 \theta)$, with scale factor $a(\eta) = c\eta$, which is known as the metric of the Milne universe (cf., e.g., Equation (16.15) of Rindler 2006). For a test particle with constant radial velocity v , we have $r = c\beta t$, where $\beta = v/c$. Using Equation (155) this yields

$$\xi = \text{arctanh} \beta, \quad \eta = \gamma^{-1} t, \quad (156)$$

where $\gamma = 1/\sqrt{1 - \beta^2}$ is the Lorentz factor. Hence, η is the proper time of the particle and ξ its rapidity. At any time t , the ejecta shell can be assigned a Milne universe with velocity $v = v_{\text{ej}}$ at $r = R_{\text{ej}}$ by appropriately rescaling the lab frame time coordinate. For the ejecta shell thickness is typically sufficiently small, i.e., $\Delta_{\text{ej}} \ll R_{\text{ej}}$, at any given time we can describe the ejecta as a thin shell in this Milne universe, which is what we call the comoving frame at time t .

First, we determine the three-acceleration a in the lab frame in terms of the corresponding quantity α in the comoving frame (cf. Equation (95)). The four-acceleration of a particle in the comoving frame is given by $A'^\mu = d^2 X'^\mu / d\eta^2 = (\gamma'^4 \alpha v' / c, \gamma'^2 (\gamma'^2 \alpha v' v'^i / c^2 + \alpha^i))$, where $v'^i = (v'^\xi, v'^\theta, v'^\phi)$ is the three-velocity, $\alpha^i = dv'^i / d\eta$, $v' = \sqrt{g'_{ij} v'^i v'^j}$, and $\alpha = dv' / d\eta$. For the fluid in the ejecta shell, $v' = v'^i = \alpha^\theta = \alpha^\phi = 0$. Hence,

$$A'^\mu = (0, \alpha^\xi, 0, 0), \quad (157)$$

$$v' = c\eta v'^\xi, \quad (158)$$

$$\alpha = c\eta \alpha^\xi. \quad (159)$$

Analogously, in the lab frame the four-acceleration is given by $A^\mu = (\gamma^4 a v / c, \gamma^2 (\gamma^2 a v v^i / c^2 + a^i))$, where $v^i = (v^r, v^\theta, v^\phi)$ is the three-velocity, $a^i = dv^i / dt$, $v = \sqrt{g_{ij} v^i v^j}$, and $a = dv / dt$. Using $v^\theta = v^\phi = a^\theta = a^\phi = 0$, we obtain

$$A^\mu = (\gamma^4 a v / c, \gamma^4 a, 0, 0). \quad (160)$$

Moreover, using Equations (157), (159), (155), and (156), we have $A^r = (\partial X^r / \partial X'^\xi) A'^\xi = (\partial r / \partial \xi) \alpha^\xi = \gamma \alpha$ and thus we obtain the desired expression (cf. Equation (95))

$$a = \frac{dv}{dt} = \gamma^{-3} \alpha. \quad (161)$$

Second, we determine the transformation of area, volume, and internal energy. Henceforth, “com” refers to the comoving frame. The surface area of spheres of radius r and corresponding rapidity ξ centered around $r = \xi = 0$ are invariant under

the transformation between lab and comoving frames:

$$\begin{aligned} S_\xi &= c^2 \eta^2 \sinh^2 \xi \int \sin \theta d\theta d\phi \\ &= 4\pi c^2 \eta^2 \sinh^2 \xi = 4\pi r^2 = S_r. \end{aligned} \quad (162)$$

The corresponding spherical volumes transform as follows:

$$V_{\text{com}}(\xi) = c^3 \eta^3 \int \sin \theta d\theta d\phi \int_0^\xi \sinh^2 \xi d\xi \quad (161a)$$

$$= \pi c^3 \eta^3 \int_0^{2\xi} (\cosh z - 1) dz = \pi c^3 \eta^3 (\sinh 2\xi - 2\xi) \quad (161b)$$

$$= \frac{4}{3} \pi r^3 \zeta = \zeta V(r), \quad (161c)$$

where

$$\zeta = \frac{3 \sinh 2\xi - 2\xi}{4 \sinh^3 \xi} = \frac{3 \gamma^2 \beta - \text{arctanh} \beta}{2 \gamma^3 \beta^3}. \quad (162)$$

Note that our definition of ζ differs from $\zeta(\beta)$ defined in Li (2013) by a factor $\gamma^{-1} = (\cosh \xi)^{-1}$. For the volume of the ejecta shell we thus find:

$$V_{\text{ej,com}} = V_{\text{com}}(\xi_{\text{ej}}) - V_{\text{com}}(\xi_{\text{n}}) = \zeta V(R_{\text{ej}}) - \zeta V(R_{\text{n}}) = \zeta V_{\text{ej}}. \quad (163)$$

In order to compute the transformation of total energy of a fluid, let $T_{\mu\nu} = (e + p)u^\mu u^\nu / c^2 + p g_{\mu\nu}$ denote the part of the energy momentum tensor excluding kinetic and rest-mass energy, with e being the internal energy density, p being the pressure, u^μ being the four-velocity, and $g_{\mu\nu}$ being the metric of flat spacetime. The total energy density as seen by a normal (Eulerian) observer with four-velocity n^μ perpendicular to the hypersurfaces of constant time t in the Minkowski spacetime is given by $e_{\text{tot}} = T_{\mu\nu} n^\mu n^\nu = \gamma^2 e + (\gamma^2 - 1)p$. For a mixture of ideal gas and radiation, we can rewrite e_{tot} as

$$\begin{aligned} e_{\text{tot}} &= \frac{1}{3} (4\gamma^2 - 1) e_r \\ &+ [\gamma^2 + (\gamma^2 - 1)(\Gamma - 1)] e_f = \frac{1}{3} (4\gamma^2 - 1) e, \end{aligned} \quad (164)$$

where e_r and e_f refer to the internal energy density of the radiation field and the gas, respectively. In the second equality in Equation (164) we have assumed an ideal gas with adiabatic index $\Gamma = 4/3$ (as for the ejecta material we consider). Consequently, the total energy of the fluid (apart from kinetic and rest-mass energy) in a spherical volume as measured in the comoving frame is given by (see Equation (161b))

$$E_{\text{com}} = e_{\text{tot,com}} V_{\text{com}} = \pi c^3 \eta^3 (\sinh 2\xi - 2\xi) e, \quad (165)$$

whereas in the lab frame it is given by $E = 4\pi \int e_{\text{tot}} r^2 dr$, which after some manipulations can be rewritten as

$$E = \frac{4}{3} \pi \eta^3 c^3 \sinh^3 \xi e. \quad (166)$$

Hence (see Equations (162) and (161)),

$$\frac{E_{\text{com}}}{E} = \zeta = \frac{V_{\text{com}}}{V}. \quad (167)$$

Thanks to Equation (163), this transformation also holds for shell volumes.

Finally, we discuss how luminosities transform between the lab and the comoving frame. Let L denote the luminosity of thermal radiation originating from the surface of the ejecta shell. Then using Equation (162), $L_{\text{com}} = S_{\zeta_{\text{ej}}} \sigma T_{\text{eff,com}}^4 = 4\pi R_{\text{ej}}^2 \sigma T_{\text{eff,com}}^4$, where $T_{\text{eff,com}} \simeq (16/3)T_{\text{com}}^4/(\Delta\tau_{\text{com}} + 1)$ is the effective temperature at optical depth $\Delta\tau_{\text{com}}$ in the comoving frame. The energy loss ΔE_{com} associated with this luminosity as measured in the comoving frame during a time $\Delta\eta$ is given by $\Delta E_{\text{com}} = L_{\text{com}} \Delta\eta = L_{\text{com}} \gamma^{-1} \Delta t$, where we have used Equation (156) and γ denotes the Lorentz factor of the ejecta shell. The corresponding energy loss as measured in the lab frame is then obtained as (cf. Equation (167)) $L \Delta t = \Delta E = \zeta^{-1} \Delta E_{\text{com}} = \zeta^{-1} \gamma^{-1} L_{\text{com}} \Delta t$. Hence, we arrive at

$$L = \zeta^{-1} \gamma^{-1} L_{\text{com}}, \quad (168)$$

which is the desired result to motivate Equations (100) and (101).

A.3. Synchrotron Emission

This appendix derives the relevant expressions needed to include effects of synchrotron emission into our model of the PWN in Phase III (Equations (86)–(88)). The spontaneously emitted spectral power at frequency ν of a single particle of charge q , mass m , and Lorentz factor γ , accelerated by a magnetic field of strength B , is given by (Crusius & Schlickeiser 1986; Rybicki & Lightman 2004)

$$p(\nu, \theta, \gamma) = \frac{\sqrt{3} q^3 B}{mc^2} \sin \theta \frac{\nu}{\tilde{\nu}_c} \int_{\nu/\tilde{\nu}_c}^{\infty} K_{\frac{5}{3}}(z) dz, \quad (169)$$

where c is the speed of light, θ is the angle between the magnetic field and the direction of particle motion, $K_{\frac{5}{3}}$ denotes the modified Bessel function of order $5/3$, and $\tilde{\nu}_c = \nu_c \sin \theta = (3/4\pi)(qB\gamma^2/mc) \sin \theta$. Assuming an isotropic distribution of particle velocities, we can average over all possible angles for a given speed γ to obtain the average energy loss rate for a particle (cf. Crusius & Schlickeiser 1986):

$$\begin{aligned} p(\nu, \gamma) &= \frac{1}{4\pi} \int_0^{2\pi} d\phi \int_0^{4\pi} d\theta \sin \theta p(\nu, \theta, \gamma) \\ &= \frac{\sqrt{3} q^3 B}{mc^2} \mathcal{R}(\nu/\nu_c), \end{aligned} \quad (170)$$

where

$$\mathcal{R}(z) = \frac{\pi}{2} z \left[W_{0, \frac{4}{3}}(z) W_{0, \frac{1}{3}}(z) - W_{\frac{1}{2}, \frac{5}{6}}(z) W_{-\frac{1}{2}, \frac{5}{6}}(z) \right]. \quad (171)$$

Here, $W_{\lambda, \mu}(z) = e^{-\frac{1}{2}z} z^{\frac{1}{2} + \mu} U(0.5 + \mu - \lambda, 1 + 2\mu, z)$ is the Whittaker function and U denotes the confluent hypergeometric function of second kind (Abramowitz & Stegun 1972, Section 13.1). Substituting ν with the dimensionless energy $x = h\nu/mc^2$, with h being the Planck constant, one has the relation $p(x, \gamma) = (mc^2/h)p(\nu, \gamma)$; accordingly, we define $x_c = h\nu_c/mc^2$. Therefore we can write the total cooling rate $\dot{\gamma}$

of a single particle as

$$\dot{\gamma}(\gamma) = -\frac{1}{mc^2} \int p(x, \gamma) dx = -\frac{\sqrt{3} q^3 B}{hmc^2} \int \mathcal{R}(x/x_c) dx. \quad (172)$$

Furthermore, the number density of photons emitted per unit time and per unit normalized energy x is given by

$$\begin{aligned} \dot{n}(x) &= \frac{1}{mc^2 x} \int N(\gamma) p(x, \gamma) d\gamma \\ &= \frac{\sqrt{3} q^3 B}{hmc^2} \frac{1}{x} \int N(\gamma) \mathcal{R}(x/x_c) d\gamma, \end{aligned} \quad (173)$$

where $N(\gamma)$ is the particle density per normalized energy γ . Finally, assuming a uniform opacity coefficient the optical depth $\Delta\tau$ to synchrotron self-absorption for a spherical volume of radius R is given by (Ghisellini et al. 1988; Ghisellini & Svensson 1991)

$$\Delta\tau(\nu) = \frac{R}{8\pi m\nu^2} \int \frac{N(\gamma)}{\gamma\alpha} \frac{\partial}{\partial t} [\gamma\alpha p(\nu, \gamma)] d\gamma, \quad (174)$$

where $\alpha = \sqrt{\gamma^2 - 1}$. Using the information from above, Equation (174) can be rearranged to give

$$\begin{aligned} \Delta\tau(x) &= \frac{\sqrt{3} q^3 h^2 BR}{8\pi m^4 c^6} \\ &\times \frac{1}{x^2} \int N(\gamma) \left[\frac{\partial}{\partial \gamma} \mathcal{R}(x/x_c) + f(\gamma) \mathcal{R}(x/x_c) \right] d\gamma, \end{aligned} \quad (175)$$

where $f(\gamma) = (2\gamma^2 - 1)/[\gamma(\gamma^2 - 1)]$, with $\lim_{\gamma \rightarrow 1} f(\gamma) = 2$.

A.4. Energy Conservation in the Nebula

This appendix demonstrates that Equations (78) and (79) conserve energy. Integrating Equation (78) the total energy balance per unit volume per unit time is given by

$$\begin{aligned} \int \dot{n}_{\text{esc}} x dx &= \int \dot{n}_{0,x} dx + \int \dot{n}_{A,x} dx \\ &+ \int \dot{n}_{\text{C}}^{\text{NT}} x dx + \int \dot{n}_{\text{C}}^{\text{T}} x dx \\ &+ \int \dot{n}_{\text{syn}} x dx - \frac{c}{R_n} \int n \Delta\tau_{\text{C}}^{\text{NT}} x dx \\ &- \frac{c}{R_n} \int n \Delta\tau_{\gamma} x dx. \end{aligned} \quad (176)$$

From Equation (83) we have

$$\begin{aligned} &- \int_1^{\gamma_{\text{max}}} \dot{\gamma}_{\text{C,syn}}(\gamma) N(\gamma) d\gamma \\ &= \frac{\sqrt{3} e^3 B}{hmc^2} \int_1^{\gamma_{\text{max}}} d\gamma \int dx N(\gamma) \mathcal{R}(x/x_c) \\ &- \int_1^{\gamma_{\text{max}}} \dot{\gamma}_{\text{C}} N(\gamma) d\gamma \\ &= \int \dot{n}_{\text{syn}} x dx - \int_1^{\gamma_{\text{max}}} \dot{\gamma}_{\text{C}} N(\gamma) d\gamma, \end{aligned} \quad (177)$$

and hence

$$\int \dot{n}_{\text{syn}} x dx = \int_1^{\gamma_{\text{max}}} [Q(\gamma) + P(\gamma)](\gamma - 1) d\gamma + \int_1^{\gamma_{\text{max}}} \dot{\gamma} c N(\gamma) d\gamma. \quad (178)$$

Plugging this into Equation (176) and noting that the second term on the right hand side of Equation (178) cancels the third and sixth term on the right hand side of Equation (176) (see LZ87, Appendix A), we can proceed as in Appendix A of LZ87 to conclude that

$$\int \dot{n}_{\text{esc}} x dx = \int \dot{n}_0 x dx + \int_1^{\gamma_{\text{max}}} Q(\gamma)(\gamma - 1) d\gamma. \quad (179)$$

Therefore, the total injected power equals the total power output, which shows that energy is conserved in steady state.

REFERENCES

- Aasi, J., Abbott, B. P., Abbott, R., et al. 2014, *PhRvL*, **113**, 011102
- Abadie, J., Abbott, B. P., Abbott, R., et al. 2012a, *A&A*, **541**, A155
- Abadie, J., Abbott, B. P., Abbott, R., et al. 2012b, *ApJ*, **760**, 12
- Abramowicz, M. A., Novikov, I. D., & Paczynski, B. 1991, *ApJ*, **369**, 175
- Abramowitz, M., & Stegun, I. A. 1972, Handbook of mathematical functions with formulas, graphs and mathematical tables (Washington, DC: National Bureau of Standards)
- Accadia, T., Acernese, F., Antonucci, F., et al. 2011, *CQGra*, **28**, 114002
- Antoniadis, J., Freire, P. C. C., Wex, N., et al. 2013, *Sci*, **340**, 448
- Arons, J. 2012, *SSRv*, **173**, 341
- Atayan, A. M., & Aharonian, F. A. 1996, *MNRAS*, **278**, 525
- Barnes, J., & Kasen, D. 2013, *ApJ*, **775**, 18
- Barthelmy, S. D., Chincarini, G., Burrows, D. N., et al. 2005, *Natur*, **438**, 994
- Bauswein, A., Goriely, S., & Janka, H.-T. 2013, *ApJ*, **773**, 78
- Belczynski, K., O'Shaughnessy, R., Kalogera, V., et al. 2008, *ApJL*, **680**, L129
- Belmont, R., Malzac, J., & Marcowith, A. 2008, *A&A*, **491**, 617
- Berger, E. 2014, *ARA&A*, **52**, 43
- Berger, E., Fong, W., & Chornock, R. 2013, *ApJL*, **774**, L23
- Blumenthal, G. R., & Gould, R. J. 1970, *RvMP*, **42**, 237
- Bucciantini, N., Metzger, B. D., Thompson, T. A., & Quataert, E. 2012, *MNRAS*, **419**, 1537
- Bühler, R., & Blandford, R. 2014, *RPPh*, **77**, 066901
- Camus, N. F., Komissarov, S. S., Bucciantini, N., & Hughes, P. A. 2009, *MNRAS*, **400**, 1241
- Ciolfi, R., & Siegel, D. M. 2015a, in Proc. Swift: 10 Years of Discovery, PoS (SWIFT 10), ed. P. Cavario, P. D'Avanzo, N. Gehrels, & G. Tagliaferri (Trieste, Italy: Proceedings of Science, SISSA), 108 (http://pos.sissa.it/archive/conferences/233/108/SWIFT%2010_108.pdf)
- Ciolfi, R., & Siegel, D. M. 2015b, *ApJL*, **798**, L36
- Clark, J., Evans, H., Fairhurst, S., et al. 2015, *ApJ*, **809**, 53
- Coppi, P. S. 1992, *MNRAS*, **258**, 657
- Crusius, A., & Schlickeiser, R. 1986, *A&A*, **164**, L16
- Davies, M. B., Benz, M. B., Piran, T., & Thielemann, F. K. 1994, *ApJ*, **431**, 742
- Demorest, P. B., Pennucci, T., Ransom, S. M., Roberts, M. S. E., & Hessels, J. W. T. 2010, *Natur*, **467**, 1081
- Dessart, L., Ott, C. D., Burrows, A., Rosswog, S., & Livne, E. 2009, *ApJ*, **690**, 1681
- Duez, M. D., Liu, Y. T., Shapiro, S. L., Shibata, M., & Stephens, B. C. 2006, *PhRvD*, **73**, 104015
- Eichler, D., Livio, M., Piran, T., & Schramm, D. N. 1989, *Natur*, **340**, 126
- Evans, P. A., Fridriksson, J. K., Gehrels, N., et al. 2012, *ApJS*, **203**, 28
- Fong, W., Berger, E., Metzger, B. D., et al. 2014, *ApJ*, **780**, 118
- Fox, D. B., Frail, D. A., Price, P. A., et al. 2005, *Natur*, **437**, 845
- Gaensler, B. M., & Slane, P. O. 2006, *ARA&A*, **44**, 17
- Gao, H., Ding, X., Wu, X.-F., Dai, Z.-G., & Zhang, B. 2015, *ApJ*, **807**, 163
- Gao, H., Ding, X., Wu, X.-F., Zhang, B., & Dai, Z.-G. 2013, *ApJ*, **771**, 86
- Gehrels, N., Sarazin, C. L., O'Brien, P. T., et al. 2004, *ApJ*, **611**, 1005
- Gehrels, N., Chincarini, G., Giommi, P., et al. 2005, *Natur*, **437**, 851
- Gelfand, J. D., Slane, P. O., & Zhang, W. 2009, *ApJ*, **703**, 2051
- Ghisellini, G., Guilbert, P. W., & Svensson, R. 1988, *ApJL*, **334**, L5
- Ghisellini, G., & Svensson, R. 1991, *MNRAS*, **252**, 313
- Giacomazzo, B., & Perna, R. 2013, *ApJL*, **771**, L26
- Giacomazzo, B., Zrake, J., Duffell, P. C., MacFadyen, A. I., & Perna, R. 2015, *ApJ*, **809**, 39
- Goldreich, P., & Julian, W. H. 1969, *ApJ*, **157**, 869
- Gompertz, B. P., O'Brien, P. T., & Wynn, G. A. 2014, *MNRAS*, **438**, 240
- Gompertz, B. P., O'Brien, P. T., Wynn, G. A., & Rowlinson, A. 2013, *MNRAS*, **431**, 1745
- Guilbert, P. W., Fabian, A. C., & Rees, M. J. 1983, *MNRAS*, **205**, 593
- Harry, G. M., & LIGO Collaboration. 2010, *CQGra*, **27**, 084006
- Hotokezaka, K., Kyutoku, K., Tanaka, M., et al. 2013, *ApJL*, **778**, L16
- Kargaltsev, O., Cerutti, B., Lyubarsky, Y., & Striani, E. 2015, *SSRv*
- Kastaun, W., & Galeazzi, F. 2015, *PhRvD*, **91**, 064027
- Kennel, C. F., & Coroniti, F. V. 1984a, *ApJ*, **283**, 694
- Kennel, C. F., & Coroniti, F. V. 1984b, *ApJ*, **283**, 710
- Kiuchi, K., Kyutoku, K., Sekiguchi, Y., Shibata, M., & Wada, T. 2014, *PhRvD*, **90**, 041502
- Kotera, K., Phinney, E. S., & Olinto, A. V. 2013, *MNRAS*, **432**, 3228
- Kulkarni, S. R. 2005, arXiv:astro-ph/0510256
- Kumar, P., & Zhang, B. 2015, *PhR*, **561**, 1
- Lasota, J.-P., Haensel, P., & Abramowicz, M. A. 1996, *ApJ*, **456**, 300
- Li, L.-X. 2007, *MNRAS*, **380**, 621
- Li, L.-X. 2013, *FrPhy*, **8**, 555
- Li, L.-X., & Paczyński, B. 1998, *ApJL*, **507**, L59
- Lightman, A. P., & Zdziarski, A. A. 1987, *ApJ*, **319**, 643
- Lü, H.-J., Zhang, B., Lei, W.-H., Li, Y., & Lasky, P. D. 2015, *ApJ*, **805**, 89
- Margalit, B., Metzger, B. D., & Beloborodov, A. M. 2015, *PhRvL*, **115**, 171101
- Marti, J. M., Mueller, E., & Ibanez, J. M. 1994, *A&A*, **281**, L9
- Metzger, B. D., & Berger, E. 2012, *ApJ*, **746**, 48
- Metzger, B. D., & Fernández, R. 2014, *MNRAS*, **441**, 3444
- Metzger, B. D., & Piro, A. L. 2014, *MNRAS*, **439**, 3916
- Metzger, B. D., Quataert, E., & Thompson, T. A. 2008, *MNRAS*, **385**, 1455
- Metzger, B. D., Vurm, I., Hascöet, R., & Beloborodov, A. M. 2014, *MNRAS*, **437**, 703
- Metzger, B. D., Quataert, E., & Thompson, T. A. 2010, *MNRAS*, **406**, 2650
- Mizuno, Y., Lyubarsky, Y., Nishikawa, K.-I., & Hardee, P. E. 2011, *ApJ*, **728**, 90
- Murguía-Berthier, A., Montes, G., Ramirez-Ruiz, E., De Colle, F., & Lee, W. H. 2014, *ApJL*, **788**, L8
- Nagakura, H., Hotokezaka, K., Sekiguchi, Y., Shibata, M., & Ioka, K. 2014, *ApJL*, **784**, L28
- Narayan, R., Paczynski, B., & Piran, T. 1992, *ApJL*, **395**, L83
- Oechslin, R., Janka, H.-T., & Marek, A. 2007, *A&A*, **467**, 395
- Olmi, B., Del Zanna, L., Amato, E., Bandiera, R., & Bucciantini, N. 2014, *MNRAS*, **438**, 1518
- Olmi, B., Del Zanna, L., Amato, E., & Bucciantini, N. 2015, *MNRAS*, **449**, 3149
- Paczynski, B. 1986, *ApJL*, **308**, L43
- Paschalidis, V., Ruiz, M., & Shapiro, S. L. 2015, *ApJL*, **806**, L14
- Philippov, A. A., Spitkovsky, A., & Cerutti, B. 2015, *ApJL*, **801**, L19
- Piran, T., Nakar, E., & Rosswog, S. 2013, *MNRAS*, **430**, 2121
- Porth, O., Komissarov, S. S., & Keppens, R. 2014, *MNRAS*, **438**, 278
- Price, D. J., & Rosswog, S. 2006, *Sci*, **312**, 719
- Rees, M. J. 1966, *Natur*, **211**, 468
- Rezzolla, L., Giacomazzo, B., et al. 2011, *ApJL*, **732**, L6
- Rezzolla, L., & Kumar, P. 2015, *ApJ*, **802**, 95
- Rindler, W. 2006, Relativity: Special, General, and Cosmological (New York: Oxford Univ. Press)
- Rosswog, S. 2005, *ApJ*, **634**, 1202
- Rosswog, S., Piran, T., & Nakar, E. 2013, *MNRAS*, **430**, 2585
- Rowlinson, A., O'Brien, P. T., Metzger, B. D., Tanvir, N. R., & Levan, A. J. 2010, *MNRAS*, **409**, 531
- Rowlinson, A., O'Brien, P. T., Metzger, B. D., Tanvir, N. R., & Levan, A. J. 2013, *MNRAS*, **430**, 1061
- Rybicki, G. B., & Lightman, A. P. 2004, Radiative Processes in Astrophysics (New York: Wiley-VCH)
- Schutz, B. F. 1986, *Natur*, **323**, 310
- Shapiro, S. L. 2000, *ApJ*, **544**, 397
- Shibata, M., Duez, M. D., Liu, Y. T., Shapiro, S. L., & Stephens, B. C. 2006, *PhRvL*, **96**, 031102
- Siegel, D. M., & Ciolfi, R. 2016, *ApJ*, **819**, 15
- Siegel, D. M., & Ciolfi, R. 2015a, in Springer Proc. Phys. 170, Proc. 1st Karl Schwarzschild Meeting on Gravitational Physics 2013, ed. P. Nicolini et al. (Switzerland: Springer International Publishing)
- Siegel, D. M., & Ciolfi, R. 2015b, in Proc. Swift: 10 Years of Discovery, PoS (SWIFT 10), ed. P. Cavario, P. D'Avanzo, N. Gehrels, & P. Tagliaferri (Trieste, Italy: Proceedings of Science, SISSA), 169 (http://pos.sissa.it/archive/conferences/233/169/SWIFT%2010_169.pdf)

- Siegel, D. M., Ciolfi, R., Harte, A. I., & Rezzolla, L. 2013, *PhRvD*, **87**, 121302
- Siegel, D. M., Ciolfi, R., & Rezzolla, L. 2014, *ApJL*, **785**, L6
- Singer, L. P., Price, L. R., Farr, B., et al. 2014, *ApJ*, **795**, 105
- Spitkovsky, A. 2006, *ApJL*, **648**, L51
- Svensson, R. 1983, *ApJ*, **270**, 300
- Svensson, R. 1987, *MNRAS*, **227**, 403
- Tanaka, M., & Hotokezaka, K. 2013, *ApJ*, **775**, 113
- Tanvir, N. R., Levan, A. J., Fruchter, A. S., et al. 2013, *Natur*, **500**, 547
- Taub, A. H. 1948, *PhRv*, **74**, 328
- Troja, E., Rosswog, S., & Gehrels, N. 2010, *ApJ*, **723**, 1711
- Volpi, D., Del Zanna, L., Amato, E., & Bucciantini, N. 2008, *A&A*, **485**, 337
- Williamson, A. R., Biwer, C., Fairhurst, S., et al. 2014, *PhRvD*, **90**, 122004
- Yang, B., Jin, Z.-P., Li, X., et al. 2015, *NatCo*, **6**, 7323 (nature.com/ncomms/2015/150611/ncoms8323/full/ncomms8323.html)
- Yu, Y.-W., Zhang, B., & Gao, H. 2013, *ApJL*, **776**, L40
- Zhang, B. 2013, *ApJL*, **763**, L22
- Zhang, B., & Mészáros, P. 2001, *ApJL*, **552**, L35
- Zrake, J., & MacFadyen, A. I. 2013, *ApJL*, **763**, L12